Journal of Petroleum Science and Engineering 188 (2020) 106946

Contents lists available at ScienceDirect

Journal of Petroleum Science and Engineering

journal homepage: http://www.elsevier.com/locate/petrol

Anisotropy evolution during early maturation of organic-rich carbonates

Yair Gordin [a,*], Yossef H. Hatzor [a], Harold J. Vinegar [a,b]

[a] Department of Geological and Environmental Sciences, Ben-Gurion University of the Negev, Be'er Sheva, 84105, Israel
[b] Vinegar Technologies, LLC, Bellaire, Tx, USA

ARTICLE INFO

Keywords:
Petroleum
Oil and gas fields
Geophysical methods
Carbonate rocks
Chalk
Sedimentary rocks

ABSTRACT

The organic-rich Late Cretaceous carbonates of the Ghareb and Mishash formations are potentially both self-sourced unconventional reservoirs and high quality source rocks for conventional petroleum systems in the eastern Mediterranean region. In this study we use cores from depths ranging from 340 to 1290 m in the Shefela and Golan Heights basins in Israel, which records the diagenesis and transformation phases of organic-rich chalk into limestone. Understanding such source rocks is complicated by the fact that each formation is unique and heterogeneity is common within each formation. Moreover, *in situ* samples at various stages of maturation are rarely available. We apply the three-plug measuring technique for a vertical transversely isotropic (VTI) medium to investigate the ultrasonic wave velocity and permeability anisotropies of organic-rich chalks (ORC) within the tested sequence.

We propose that in ORC diagenesis, the characteristics and distribution of the organic matter in the rock matrix change significantly throughout burial and thermal maturation, strongly affecting the velocities. Measuring the velocity hysteresis under varying confining pressures revealed that development of soft porosity with preferred orientation plays a crucial role in the early maturation stage (TMAX of 428–434°C), particularly under low effective stresses, while it is absent in the immature stage (TMAX of 403–415°C). The sensitivity of the wave velocities at low effective stresses results in variations in velocity anisotropy, which may potentially be utilized in seismic exploration to delineate the highly-pressured 'sweet spots' in unconventional organic-rich carbonates.

1. Introduction

1.1. General background

The interest in developing unconventional oil and gas fields in the Late Cretaceous Ghareb and Mishash formations, both located in the Shefela and Golan Heights basins in Israel, motivates our laboratory investigations of the seismic anisotropy of these rocks. These formations have the potential of being both self-sourced unconventional reservoirs and significant source-rocks for conventional petroleum systems in the region. The Ghareb and Mishash formations consist mainly of fine-grained carbonates with high concentrations of organic matter. The lithology of these rocks is mostly chalk, with occurrences of cherts, marls, porcelanites and phosphorites (Gvirtzman et al., 1989; Meilijson et al., 2014). These formations typically show sedimentary layering and complex networks of organic matter and minerals. Evidence of mechanical and petrophysical anisotropy has been recognized in previous studies of immature organic-rich chalk (ORC) from the Shefela basin (Bisnovat et al., 2015; Shitrit et al., 2016). In this paper we discuss the ultrasonic and permeability anisotropy of these formations based on laboratory investigations of the immature organic-rich chalk (ORC) from the Shefela basin of central Israel and the early-matured samples from the southern Golan Heights basin in northern Israel. The thermal maturation along the Golan section was evaluated by Rosenberg et al. (in preparation), who found that maturation increases with depth up to the stage of maximum bitumen generation.

A detailed description of the degree of seismic anisotropy is crucial to improve imaging and depth estimation when seismic methods are used (Dewhurst et al., 2011). Laboratory measurements may help determine the contribution of the intrinsic (fabric) anisotropy of the rock material itself and to simulate different field conditions (i.e. stress regime, altering pore fluid, etc.). The description of the anisotropy is also useful when unconventional reservoirs are developed. For example, the anisotropy may lead to differential stresses upon loading, which could affect hydraulic stimulations (Martínez and Schmitt, 2013). Moreover, a deeper understanding of the relation between seismic rock

* Corresponding author.
E-mail address: gordiny@post.bgu.ac.il (Y. Gordin).

https://doi.org/10.1016/j.petrol.2020.106946
Received 2 September 2019; Received in revised form 6 December 2019; Accepted 8 January 2020
Available online 9 January 2020

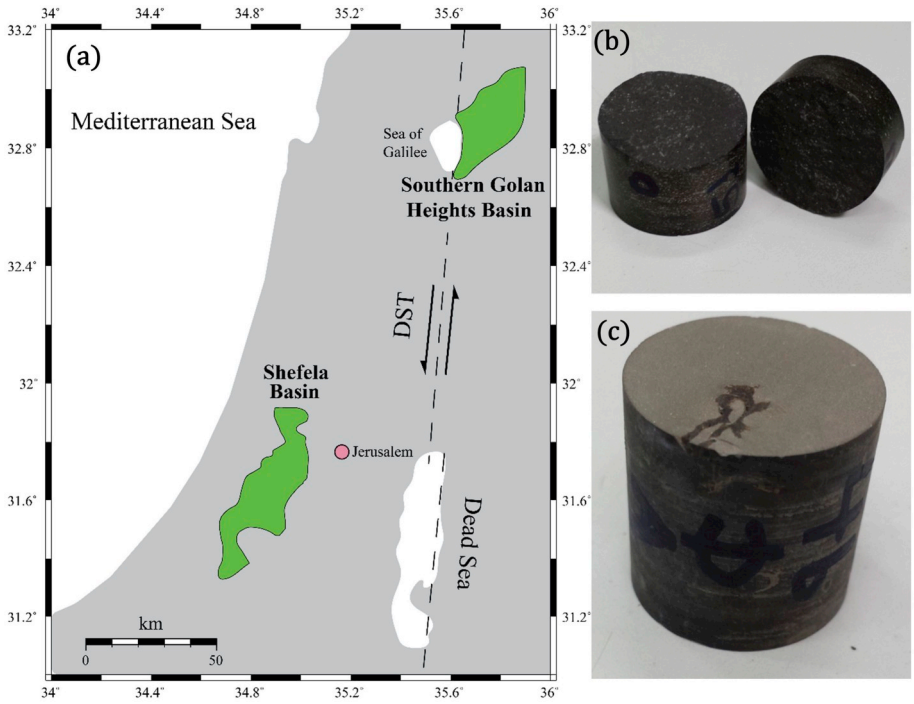

Fig. 1. (a) Map showing the geographical location of the Organic Rich Chalks (ORCs) of the southern Golan Heights and Shefela basins on both sides of the Dead Sea Transform (DST). The Shefela basin spatial extension (in green) was adopted from (Minster, 2009). (b) A vertical, broken, early-mature stage plug extracted from the Golan basin from the depth of 1051 m split across a sub-horizontal weakness plane, and (c) an immature plug from the Shefela basin from the depth of 340 m. (For interpretation of the references to color in this figure legend, the reader is referred to the Web version of this article.)

characteristics and petrophysical and geochemical properties may aid in seismic exploration for remote detection of the ORC, their maturation state and possible migration paths.

It is generally believed that at field scale, seismic anisotropy is influenced by several major factors, such as (1) layering of diverse lithologies with different elastic properties on a scale much finer than the propagating seismic wavelength, (2) the dominant directionality of minerals or organic matter, (3) fractures and microcracks with preferred alignment, and (4) *in situ* stresses regime (Koren et al., 2009; Vernik and Nur, 1992). Pervukhina and Rasolofosaon (2017) studied two large databases consisting of more than 800 samples [including data from (Horne, 2013)] and suggested that burial and compaction can be excluded as a major cause of seismic anisotropy in shale formations. They also showed that clay platelet alignment explain most of the anisotropy measurements in their studied database based on a previous study (Sayers, 2013). However, since clay minerals are sparse in our set of samples (0–3.5 %vol), we believe clays are not the main reason for the anisotropy in the ORCs. This leads us to explore other causes for the detected anisotropy.

By measuring twenty core samples from different depths and thermal maturation stages, ranging from the immature to the early maturation stages, and focusing on a set of eleven anisotropy velocity measurement samples, we discuss how burial, diagenesis, and natural thermal maturation affect the micro-structure, the velocity, and the anisotropy of the ORCs. The strategies we use in this study combine wave velocity anisotropy with petrophysical measurements (e.g. porosity, permeability, and density), XRD mineralogy, and SEM observations. Finally, we use the Iso-Frame (IF) modeling method proposed by Fabricius (2003) to examine the rock physics evolution (e.g. compaction and cementation) of ORCs with burial and diagenesis. The IF model is an effective medium model in which the IF value quantifies, on a scale from 0 to 1, the amount of solids required to take part in the load-supporting frame of the rock, while the rest of the solids are assumed to be suspended in the pore-fluid and not to take part in supporting the rock frame. This model helps explain how the properties of the ORCs change during diagenesis, as cementation develops and porosity decreases.

1.2. Organic-rich chalks

The ORCs in this study are soft high-porosity carbonates, rich in organic matter. The matrix of the rock is composed primarily of biogenic calcitic mud mixed with kerogen. Microfossils dominate in some of the samples and are scattered throughout the rock matrix. The kerogen of the Ghareb and Mishash formation is classified as type IIS (Spiro, 1980), where 'S' indicates the sulfur-rich nature of this kerogen. The oil window of type IIS kerogen starts at earlier maturities than in other kerogens, reaches its peak at values similar to type II kerogen, and continues expelling oil at high maturities (Kutuzov, 2017). With burial, these sedimentary rocks undergo several simultaneous diagenetic processes coupled with thermal maturation, all of which strongly affect physical and mechanical behavior.

Chalks form under relatively deep marine conditions, from the gradual accumulation of calcite shells of micro-organisms, especially coccoliths and foraminifera. It is widely accepted that the physical properties of chalks are greatly influenced by burial depth. With increasing depth, the rock is subjected to higher *in situ* stresses and temperatures. These conditions enhance compaction and cementation. If organic matter is preserved post deposition, the higher temperatures can also stimulate thermal maturation of organic matter leading to the generation of hydrocarbons and their subsequent migration.

Generally, during the first stage of ORC generation, calcite shells and organic matter deposit as suspensions on the sea floor. When the sediments are buried deep enough, i.e. between 200 and 300 m, contact cementation occurs and the ooze transforms into chalk. Previous studies identified several diagenetic stages of carbonate rocks with burial depth, creating a transformation sequence of ooze to chalk to limestone (Fabricius, 2003; Grützner and Mienert, 1999). The core samples in this study represent a diagenesis from soft chalk (beginning with shallow depth of 340 m) to the chalk-limestone transformation stages (at the depth of 1290 m), simultaneously with early maturation of the kerogen.

1.3. Geological setting

Approximately thirty late Cretaceous basins containing organic-rich chalk deposits are found in Israel (Gardosh and Tannenbaum, 2014;

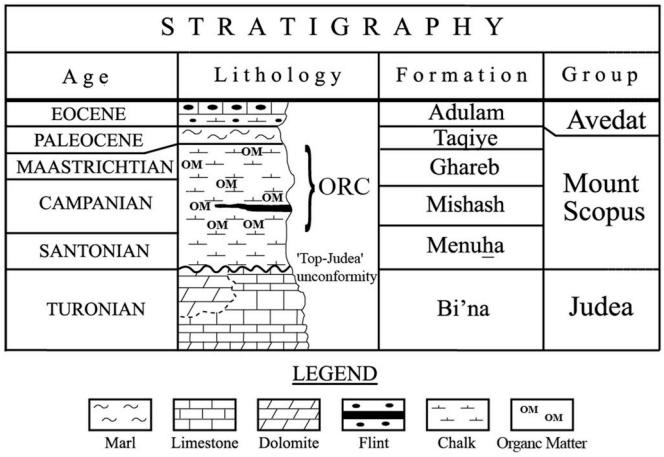

Fig. 2. Schematic composite stratigraphic column of the ORC of Mt. Scopus Group, from the Shefela and Golan regions. Not to scale (modified after Burg and Gersman, 2016; Mor et al., 1997; Mimran et al., 1985). The thickness of the ORC units varies significantly with the structural location in each basin, but is at least a few hundred meters thick in both regions.

Minster, 2009). The late Cretaceous organic-rich chalks were deposited in a series of local NE-SW trending synclinal basin structures associated with the 'Syrian Arc' folding system (Eyal and Reches, 1983). These sediments were deposited at the passive margins of the northern Arabian Plate and at the southern margins of the Tethys Ocean (Gvirtzman et al., 1989). In order to test the organic-rich chalks at different stages of burial and thermal maturity, cores were extracted from both the Shefela and southern Golan Heights basins, in central and northern Israel, respectively (Fig. 1).

The 'Syrian Arc' folding system began to develop during the Turonian-Coniacian era leaving the top of the Judea Group truncated. Since the Late Coniacian era, a new transgressive regime was established, which led to the deposition of the Late Cretaceous ORC, overlaying the mid-Cretaceous carbonates' platform and atop an erosional surface. This unconformity is commonly referred to as the 'Top-Judea' unconformity (Flexer, 1971; Meilijson et al., 2014, Fig. 2). High organic sedimentation rates accompanied by limited exposure to oxygen led to favorable preservation conditions of the organic matter. In the Shefela and Golan basins, the ORC is several hundred meters thick and is controlled by the basin structure development at the time of deposition (Gvirtzman et al., 1989; Shulman et al., 2004).

Since the Early Miocene, the Dead Sea Transform (DST) was developed as a ~1100 km long sinistral strike-slip plate boundary, which separates the Arabian plate from the Sinai subplate (Freund et al., 1970; Kaviani et al., 2013). The DST left-lateral motion accommodated ~105 km since the Middle Miocene (Freund et al., 1968; Marco et al., 2005). Consequently, the southern Golan basin, located in a proximity to the east side of the DST, shifted north in relation to the Shefela basin (see Fig. 1).

Even though both basins were originally deposited in proximity to each other (before the DST was developed) and are part of the same historical depositional environment, their geothermal and tectonic histories are quite different because of their separation across the DST (Levitte and Greitzer, 2005; Meiler et al., 2011; Minster et al., 1992; Shalev et al., 2013). In the Shefela basin, the formation lays in a syncline structure at a shallow depth (330–700 m), the chalk is dark brown (or gray), and the organic matter is immature kerogen with very little bitumen. In the Golan basin, the same formation is found at depths of 700 m–2000m, the basin is tectonically active and is highly fractured due to the proximity to the active Dead Sea Transform. The ORC in the Golan basin is black and the kerogen is partially matured with large amounts of bitumen. An early maturation broken core plug from the Golan basin is illustrated in Fig. 1b and an immature core plug from the Shefela basin is illustrated in Fig. 1c. The greater maturation in the Golan basin is a consequence of greater depth and the high geothermal gradient in the southern Golan Heights basin (3–4°C/100 m) due to extensive volcanic activity (16–0.1 Ma) in the region (Gardosh and Tannenbaum, 2014; Levitte and Greitzer, 2005; Shalev et al., 2013).

1.4. Theoretical background

We assume that the ORC formations investigated here exhibit vertical transverse isotropy (VTI) based on the horizontal layering in the field and on results of previous studies of their mechanical and petrophysical anisotropy (Bisnovat et al., 2015; Shitrit et al., 2016). A transversely isotropic material has physical properties which are equal in all directions perpendicular to the axis of symmetry but are not necessarily equal in other directions. Hooke's law for an anisotropic VTI elastic material may be described using five independent stiffness constants, relating stress to strain components. Those five elastic constants form a fourth order tensor which may be written in the Voigt notation as a twelve non zero component matrix (Mavko et al., 2019; Sarout et al., 2007):

$$C_{ij} = \begin{pmatrix} C_{11} & C_{11}-2C_{66} & C_{13} & 0 & 0 & 0 \\ C_{11}-2C_{66} & C_{11} & C_{13} & 0 & 0 & 0 \\ C_{13} & C_{13} & C_{33} & 0 & 0 & 0 \\ 0 & 0 & 0 & C_{44} & 0 & 0 \\ 0 & 0 & 0 & 0 & C_{44} & 0 \\ 0 & 0 & 0 & 0 & 0 & C_{66} \end{pmatrix}, \quad (1)$$

where $C_{11}, C_{33}, C_{44}, C_{66}$ and C_{13} are the five independent elastic constants needed to describe a VTI medium.

In order to estimate the elastic constants needed to fully describe transversely isotropic media, the elastic constants can be expressed as follows (Carcione, 2007; Lo et al., 1986; Mavko et al., 2019):

$$\begin{aligned} &C_{11} = \rho_b V_P(90\ ^\circ)^2\ ;\ C_{33} = \rho_b V_P(0\ ^\circ)^2 \\ &C_{44} = \rho_b V_S(0\ ^\circ)^2\ ;\ C_{66} = \rho_b V_{SH}(90\ ^\circ)^2 \\ &C_{13} = \sqrt{\left(2\rho_b V_P(45\ ^\circ)^2 - C_{11} - C_{44}\right)\left(2\rho_b V_P(45\ ^\circ)^2 - C_{33} - C_{44}\right)} - C_{44} \end{aligned} \quad (2)$$

where ρ_b is the bulk density, V is the velocity, and the subscripts P, S, and SH refer to the P-wave, S-wave, and horizontally polarized S-wave, respectively. These equations allow us to estimate the elastic constants using the ultrasonic wave velocities at different wave propagation directions. The elastic constants C_{11}, C_{33}, C_{44} and C_{66} can be determined relatively easily by measuring wave velocity along the horizontal and vertical axes of the material. Determination of C_{13} from ultrasonic velocity measurements at 45° or other off-axis measurements, is more complicated and introduces significant uncertainties requiring special attention (Chichinina, 2017; Dewhurst et al., 2011; Sarout et al., 2014; Yan et al., 2016). From the elastic constants, three dimensionless anisotropy parameters introduced by Thomsen can be calculated for a VTI medium (Thomsen, 1986):

$$\begin{aligned} \varepsilon &= \frac{C_{11} - C_{33}}{2C_{33}}, \\ \gamma &= \frac{C_{66} - C_{44}}{2C_{44}}, \\ \delta &= \frac{(C_{13} + C_{44})^2 - (C_{33} - C_{44})^2}{2C_{33}(C_{33} - C_{44})}, \end{aligned} \quad (3)$$

where ε and γ are parameters used to quantify the P-wave and S-wave anisotropy, respectively, and δ controls the angular dependence anisotropic response of the wave velocity at the near-vertical angle and may be either negative or positive (Thomsen, 1986; Tsvankin, 1997). Determination of δ requires the use of the elastic moduli C_{13}, thus suffers major uncertainties. Although this issue is beyond the scope of this

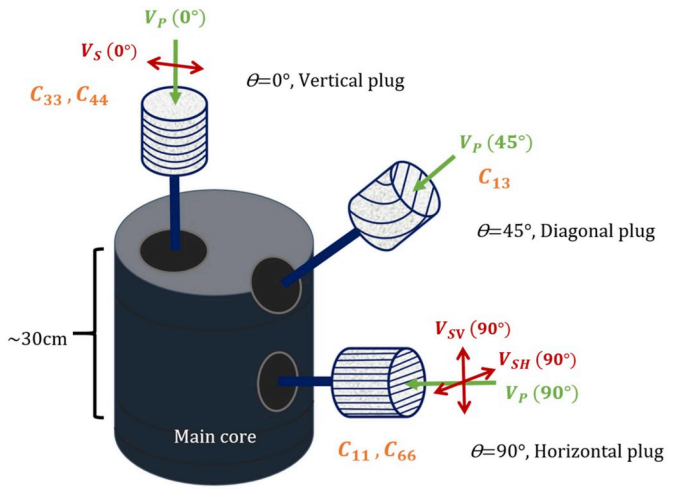

Fig. 3. For each depth interval, three plugs were cut from the main core. The different directions of wave velocity measurements are shown: Green arrows represent directions of compressional and shear wave propagation through the sample plugs, and red arrows represent directions of S-wave particle motion. The velocities were used to estimate the five elastic constants (shown in orange) for a vertical transversely isotropic medium (VTI). (For interpretation of the references to color in this figure legend, the reader is referred to the Web version of this article.)

paper, calculated values of δ and C_{13} are presented in the results section.

In addition to the determination of the rock fabric anisotropy, by changing the effective confining pressure during ultrasonic wave measurements in different directions, microcracks (or soft porosity) can be detected and their preferred orientation can be inferred (Allan et al., 2016, 2015; 2014; Meléndez-Martínez and Schmitt, 2016). Raising the confining pressure sufficiently will close microcracks, causing the velocity to increase sharply. Measuring the velocities using a wide range of confining pressures enables us to determine the degree of anisotropy covering a wide range of *in situ* effective stresses. At high stresses, as compliant microcracks close, the remaining velocity anisotropy represents the anisotropy of the rock fabric itself without the contribution of the microcracks. The closure of microcracks stiffens the rock frame and increases the acoustic velocities.

2. Methodology

2.1. Sample preparation

In order to describe the elastic moduli of a transversely isotropic rock, velocity measurements must be determined at a minimum of three different directions with respect to the bedding orientation. For that reason, samples were cut from the main core into vertical (V, 0°), horizontal (H, 90°) and diagonal (D, 45°) plugs, with respect to the core axis, assuming that the perpendicular and parallel to bedding directions are aligned with the vertical and horizontal core directions (based on optical observations of the cores, Fig. 3). The cylindrical plugs were 25.4 mm (1″) diameter by 25.4 mm (1″) length, and their edges were polished parallel to each other. The plugs were oven dried at 110°C to avoid the influence of pore fluid chemistry on the measurements (Vernik and Landis, 1996) and the samples were weighed every few hours to check for an asymptotic weight to ensure dry conditions. No attempt was made to remove bitumen from the samples.

The possible inhomogeneity between the plugs is one of the main disadvantages of the three-plug method. To address this issue, measurements of density, porosity, and XRD were performed for each core to confirm homogeneity. The samples with the greatest similarity (less than 3% relative difference in density and porosity) were selected for the velocity anisotropy analysis. Furthermore, only cores retrieved from calcite-rich zones were used in this study while cores from silica-rich zones, with complex and heterogeneous texture, were excluded due to their heterogeneity and the inapplicable nature of the anisotropy assessment at high frequency (short wavelength) acoustic velocity tests.

2.2. Petrophysical measurements

Petrophysical, mechanical and geochemical properties were measured once all plugs were cut from the main cores and dried. First, the dimensions of the plugs were measured, the plugs were weighed, and bulk density was calculated by dividing mass by volume, with accuracy of ±0.01 g/cm3 (Table 1). Then, the three cylindrical plugs for each core (in 0°, 45° and 90° directions) were used to measure the effective porosity, Klinkenberg-corrected (equivalent liquid) permeability for nitrogen gas, and solids density, using the Coreval-30 poro-permeameter (Vinci Technologies). During the Coreval-30 measurements, the plugs were subjected to 400 psi confining stress. The total porosity and grain density of each sample were estimated using a mass-balance approach and from a combination of several analyses: XRD-derived mineralogy, TOC, bulk density, and knowledge of the bitumen fraction of the organic matter from two previous studies (Kutuzov, 2017; Shitrit et al., 2017). The total porosity in this study refers to both the volume of empty pores and volume of pores filled with bitumen as illustrated in Fig. 4.

2.3. XRD analysis

Irregular pieces from the edges of the extracted plug samples were used for chemical characterization and mineralogical analysis using X-ray diffraction (XRD) performed at the Ilse Katz Institute for Nanoscale Science & Technology at Ben-Gurion University of the Negev (BGU). Phase identification was performed using a Bede ZDS computer match program coupled with the ICDD (International Centre for Diffraction Data) Powder Diffraction File database.

Table 1
Fundamentals of the core samples: depth, basin, maturation stage, Coreval effective porosity, calculated total porosity, bulk density, and TOC. Bulk density errors are ±0.01 g/cm3, and measured porosity errors are ±0.5%. * indicates approximate T_{MAX} values. T_{MAX} values courtesy of Rosenberg et al. (in prep.).

Sample No.	Depth [m]	Basin	Maturation stage	T_{MAX} [°C]	Coreval Effective Porosity [%]	Total Porosity [%]	Bulk density [g/cc]	TOC [wt. %]
1	400	Shefela	Immature	415*	38.1	42.2	1.49	10.0
2	462			410 *	36.3	38.5	1.45	13.3
3	515			403	35.8	34.7	1.58	9.7
4	553			410	28.8	32.5	1.67	11.65
5	913	Golan	Intermediate level	423	28.1	30.1	1.72	9.2
6	920			424	27.3	29.2	1.69	11.5
7	1031		Early maturation	428	2.8	17.8	2.07	11.6
8	1039			429	9.9	18.6	2.10	8.4
9	1059			429	13.9	17.1	2.18	5.1
10	1198			434	0.3	9.8	2.43	4.4
11	1280			429	1.2	13.9	2.29	5.5

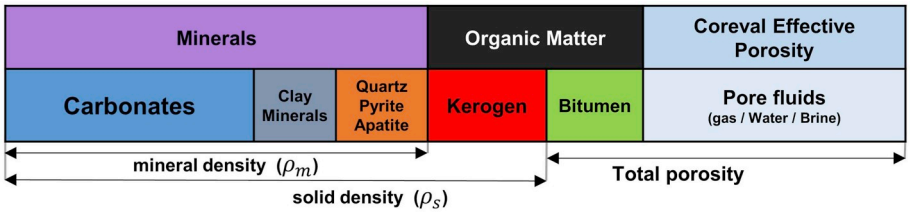

Fig. 4. Schematic presentation of the organic-rich chalk phases. The total porosity in this study refers to both the empty porous volume in the rock and the bitumen occupied porosity.

2.4. Rock-Eval pyrolysis

Rock-Eval pyrolysis of the organic material was performed using the Rock-Eval 6 system (Vinci Technologies) at the Organic Geochemistry Laboratory at BGU by Rosenberg et al. (in prep.), who showed that the gradual increase in T_{MAX} values with depth indeed represents thermal maturation. The total organic carbon (TOC) and Rock-Eval T_{MAX} are provided in Table 1. Here we only use the T_{MAX} to represent the stage of maturation of the organic matter. In order to study the effect of organic maturation on the rock properties and for simplification, we divided the cores into three main groups of different thermal maturation stages: immature (T_{MAX} of 403–415°C, see Table 1), early maturation - entering the oil window stage (T_{MAX} of 428–434°C), and an intermediate level in between the immature and early maturation stages (T_{MAX} of 423–424°C).

2.5. Ultrasonic measurements

Ultrasonic velocities were measured using an acoustic velocity system (AVS350, Vinci Technologies), using piezoelectric crystals (0.5 MHz central frequency) to generate both compressional (P) and polarized shear (S) waves. In order to calculate the velocities, the sample length was divided by the travel time of the wave through the plugs, and a correction was made to eliminate the time in which the waves traveled through the steel end caps. Wave velocities were measured using dry samples with increasing confining pressure from 2.5 MPa to 35 MPa, followed by depressurization to 2.5 MPa checking for hysteresis. The first wave arrival was acquired every 2.5 MPa below 10 MPa and every 5 MPa above 10 MPa. The accuracy of the velocity measurements is approximately 1%–2.2% for P-wave and 3.2%–6.5% for S-wave, where the accuracy improves with increasing confining pressure.

The length and diameter of each core plug were measured before and after applying confining pressure of 35 MPa. When significant contraction occurred due to the applied pressure, length corrections were made. These corrections were needed especially in the shallower depth samples where significant contraction was observed (see Section 3.2). The normal strain was calculated by dividing the difference between the initial and final lengths of the core plug by its initial length.

As illustrated in Fig. 3, six different wave velocities were measured for each core sample. One P-wave was measured in diagonal (D) plugs, Vp (45°), where the axis of the plug is inclined 45° with respect to bedding planes. One P-wave velocity, Vp (0°) and one S-wave velocity, Vs (0°) were measured in the vertical (V) plugs, where the axis of the plug is 90° with respect to bedding plane. One P-wave velocity, Vp (90°) and two polarized S-wave velocities, Vsv (90°) and VsH (90°) were measured in the horizontal (H) plugs, where the axis of the plug is parallel to the bedding planes. Since the polarization of the S-wave transducers is controlled by their orientation, a horizontally polarized S-wave, VsH (90°) was measured when the direction of the rock solid particles motion was parallel to bedding. Correspondingly, a vertical polarized S-wave Vsv (90°) was obtained when the direction of the rock solid particles motion was perpendicular to bedding (Fig. 3).

2.6. SEM observations and EDS analysis

Polished, thin sections from the edges of each plug were used for back-scattered scanning electron microscopy (BSE-SEM) using the FEI Quanta-200 at the Ilse Katz Institute for Nanoscale Science & Technology. Thin sections were studied to determine the source of the observed vertical transverse isotropy and to better understand the diagenesis with burial depth (e.g. porosity reduction, pore-filling cementation, and pressure dissolution textures). Energy dispersive X-ray spectroscopy analysis (EDS) was used during SEM for identifying the various minerals and kerogen in the sample at microscale resolution.

2.7. Conceptual rock physics models

The Iso-Frame (IF) model was proposed by Fabricius (2003) based on the Hashin-Shtrikman bounds (Hashin and Shtrikman, 1963) and the modified upper Hashin-Shtrikman (MUHS) bounds presented by Nur et al. (1995) who introduced a new term – the "Iso-Frame Values". The IF model is an effective medium model in which the IF Value quantifies, on a scale from 0 to 1, the amount of solids required to take part of the load-supporting frame of the rock. The rest of the solids are assumed to be suspended in the pore-fluid and do not to take part in supporting the rock frame. This model helps explain how the properties of the ORCs change during diagenesis, as cementation develops and porosity decreases. Using the velocity measurements in the vertical and horizontal directions, combined with the IF method, we can estimate how much of the solid phases (minerals and kerogen) are required to be embedded in the supporting frame in these orthogonal directions. The following equations were used to present the IF curves in the discussion section (Fabricius et al., 2007a, 2007b):

$$K^{HS+} = \left(\frac{\phi + (1-IF)(1-\phi)}{K_{sus} + \frac{4}{3} G_{VRH[cal+ker]}} + \frac{IF(1-\phi)}{K_{VRH[cal+ker]} + \frac{4}{3} G_{VRH[cal+ker]}} \right)^{-1} - \frac{4}{3} G_{VRH[cal+ker]}$$

$$G^{HS+} = \left(\frac{\phi + (1-IF)(1-\phi)}{\zeta} + \frac{IF(1-\phi)}{G_{VRH[cal+ker]} + \zeta} \right)^{-1} - \zeta \quad (4)$$

$$\zeta = \frac{G_{VRH[cal+ker]}}{6} \left(\frac{9K_{VRH[cal+ker]} + 8G_{VRH[cal+ker]}}{K_{VRH[cal+ker]} + 2G_{VRH[cal+ker]}} \right),$$

where IF is the Iso-Frame value, the sub-script 'sus' represents the suspension phase, and the sub-script $VRH[cal+ker]$ represents the calculation of Voigt–Reuss–Hill averaging for a mixture of calcite and kerogen, representing the rock supportive phases.

3. Results

The main goal of this study is to explore the evolution of organic-rich chalks' permeability and acoustic anisotropy during burial depth, diagenesis, and thermal maturation. The methodology includes laboratory core analysis of eleven representative core samples extracted from different depths at various thermal maturation stages, from the

Table 2
XRD-derived mineralogy for each sample [wt. %].

Sample no.	Depth [m]	Mineralogy via XRD [%]					
		Calcite	Quartz	Pyrite	Apatite	Clay	Dolomite
1	400	81.7	3	0.8	8.5	4	2
2	462	73.5	3	0	16.5	3	4
3	515	79	3	1	4.3	4.7	8
4	553	83	1.5	1	12.5	1	1
5	913	82.5	3	1	9	3	1.5
6	920	88	1.6	1	6.4	3	trace
7	1031	79	2	trace	10	6	3
8	1039	90	2	1	5	2	trace
9	1059	87	2.5	1.5	5	4	trace
10	1198	73.5	2.5	trace	11	trace	13
11	1280	87	1	0.5	5.5	trace	6

Table 3
The three main groups of components presented in the ternary diagram in Fig. 4: carbonates, clay + kerogen, and QPA (quartz, pyrite, and apatite) [%vol].

Depth [m]	Carbonates	Clay + kerogen	QPA
340	78.4	14.7	6.9
359	78.3	14.8	6.9
386	75.0	12.3	12.7
400	73.6	17.0	9.4
430	57.6	32.8	9.6
457	69.7	22.8	7.5
462	62.9	25.7	11.5
489	54.7	34.9	10.5
510	61.9	30.4	7.7
515	62.3	24.4	13.3
539	64.4	28.5	7.0
553	60.8	27.6	11.7
913	61.9	26.2	11.9
920	51.1	34.3	14.5
1031	61.4	28.1	10.5
1039	48.6	42.1	9.3
1059	54.4	35.2	10.4
1198	62.8	25.1	12.0
1280	65.4	22.0	12.6
1289	62.4	25.6	12.0

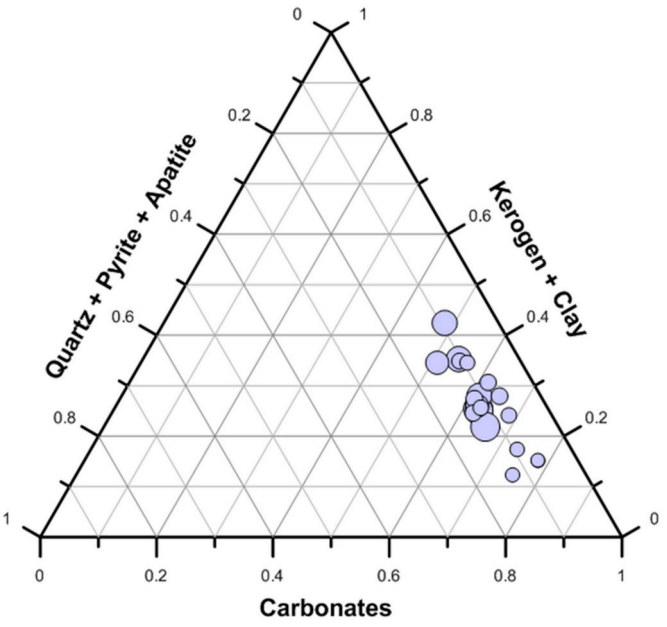

Fig. 5. Ternary diagram showing the three main groups of solid components present in our ORC data set: carbonates, kerogen and clay, and QPA (quartz, pyrite and apatite). The depth of each sample is represented by the size of the circle (from 340 to 1289 m). The data were measured using XRD and Rock-Eval analysis.

immature to the early maturation stages.

XRD and mineralogy analyses indicate that six minerals, or mineral groups, are dominant: Calcite, Dolomite, Apatite, Quartz, Clay, and Pyrite (see Tables 2 and 3, Figs. 4 and 5). Rock-Eval pyrolysis is used to measure TOC and to define the thermal maturity stage of the samples. We divide the cores into three main groups of thermal maturation levels: immature, intermediate, and early maturation - entering the oil window stage where bitumen is the major hydrocarbon fluid (see Table 1 and Fig. 6a). The immature samples were cored from depths of 340–553 m in the Shefela basin, while the samples with intermediate and early maturation stages were cored from the Golan Heights basin at depths of 913–920 m and 1031–1289 m, respectively (Fig. 6a).

3.1. Porosity, permeability, and anisotropy variations with depth

Total porosity and P-wave anisotropy (using the Thomsen's ε definition variations) vs. depth are presented in Fig. 6a and b, respectively. The data trend of non-organic chalk porosity from two published drill sites are also presented in Fig. 6a for comparison with the Israeli ORC: (1) Atlantic Ocean deep-sea drilling project/ocean drilling project (DSDP/ODP) from Grützner and Mienert (1999), and (2) North Sea chalk samples of ODP Site 807, (Fabricius, 2003; Kroenke et al., 1991). Note that the comparison between the ORC to the Atlantic Ocean and North Sea chalks is not optimal since marine chalks exhibit high pore pressure due to the water column overlying these sediments. The depth units for these samples is therefore reported as 'meters below sea floor' (mbsf). The ORC's porosity is smaller than the two non-organic porosity in the immature section at shallow depth but the gradient is similar. In the intermediate stage the porosity values of the ORC are higher than the Atlantic Ocean samples while it is smaller than the North Sea chalk. In the early-matured samples, at depths greater than 1000 m, the ORC has lower porosity than the North Sea chalk. In Fig. 6b, the ORC have considerable elastic P-wave anisotropy (ε = 0.07–0.3), whereas anisotropy in non-organic chalk was significantly lower (ε ≤ 0.08). Furthermore, Røgen (2002) studied 15 chalk samples from six hydrocarbon-bearing chalk fields in the North Sea and found that the P- and S-wave anisotropy to be zero within the estimated error. Grützner and Mienert (1999), However, measured P-wave anisotropy of ε = −0.02–0.08 using samples from the Atlantic Ocean ODP (results are presented in Fig. 6b for comparison).

Total and effective porosity vs. depth are presented in Fig. 7a. A simple exponential regression (with $r^2 = 0.85$) fits the total porosity of the immature and early maturation stages well, but not the intermediate stage, where the porosity remains just under 30% at ~900 m depth.

The Klinkenberg-corrected gas permeability of the ORC is very low, ranging from tens of nano-Darcy up to two millidarcy. It generally decreases with depth, and often displays strong anisotropy (Fig. 7b). Nevertheless, in samples from depths greater than 1100 m, the

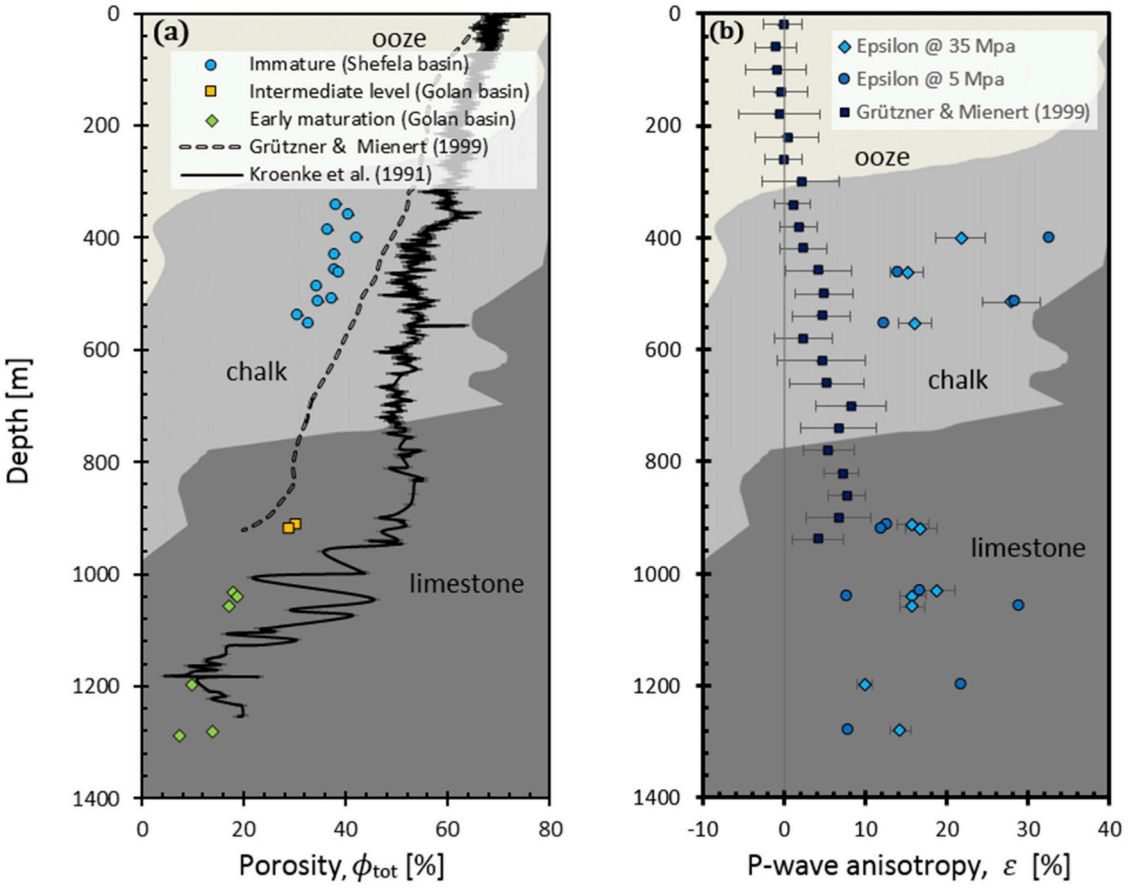

Fig. 6. The changes in the total porosity (a) and Thomsen's ε P-wave anisotropy parameter (presented in percent) (b) vs. depth in the vertical axes. Two non-organic chalk porosity trends are presented for comparison with the Israeli ORC: (1) the Atlantic Ocean deep-sea drilling project/ocean drilling project (DSDP/ODP) from Grützner and Mienert (1999), and (2) North Sea chalk samples from the ODP Site 807 (Fabricius, 2003; Kroenke, L. W. et al., 1991) with depths presented in units of meters below sea floor (mbsf). The P-wave anisotropy (ε) of the Atlantic Ocean from Grützner and Mienert (1999), black squares in (b), shows lower ε values compared to the ORC (light blue diamonds and blue circles, for measurements under 35 and 5 MPa, respectively). The background colors for the figures were modified from Grützner and Mienert (1999) and represent the relative fractions of ooze, chalk, and limestone for the Atlantic Ocean data (from core descriptions). (For interpretation of the references to color in this figure legend, the reader is referred to the Web version of this article.)

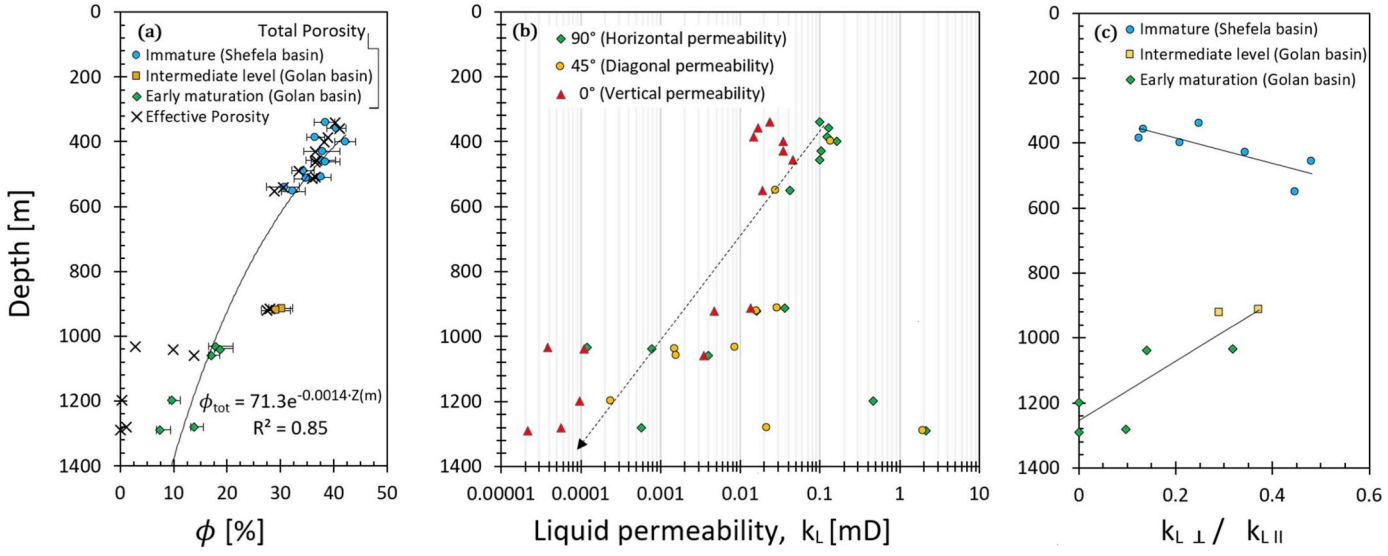

Fig. 7. (a) Total and Coreval effective porosity vs. depth. The simple exponential regression fits the total porosity of the immature and early maturation stages. However, this exponential relation is not suitable for the intermediate stage where the porosity remained just under 30%. (b) Vertical, horizontal, and 45° permeability vs. depth (permeability reduction trend marked by the dash arrow), and (c) vertical to horizontal permeability ratio vs. depth.

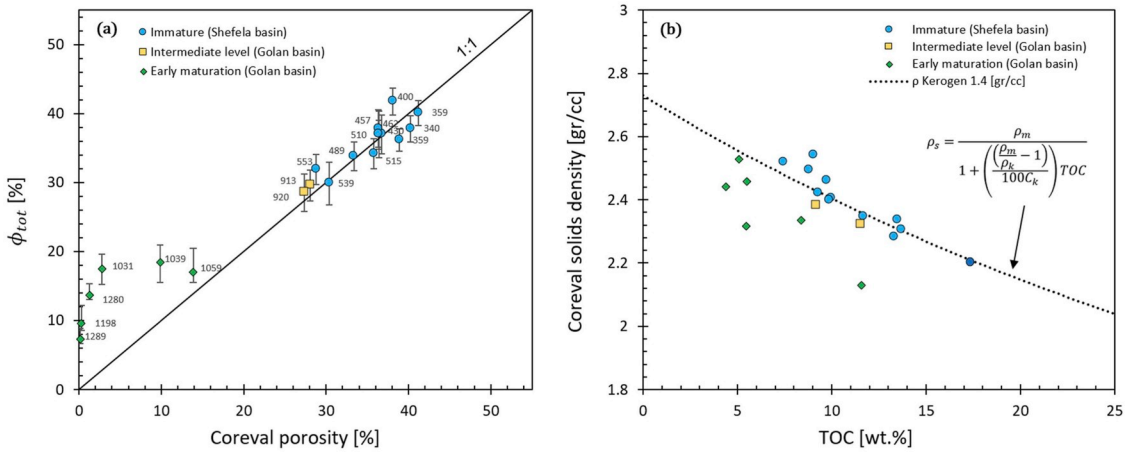

Fig. 8. A comparison of calculated total porosity and Coreval effective porosity for nitrogen gas (a). The labels of the data points represent the depth of each sample. The generation of heavy bitumen during the early-maturation stage leads to clogging of pore throats, which blocks the nitrogen gas from occupying the entire pore space. As a result, the Coreval effective porosities are less than total porosities. (b) TOC, as a function of Coreval-calculated solid density, shows an acceptable match for 1.4 g/cc density of kerogen for the immature and intermediate stages using the mass balance equation (4).

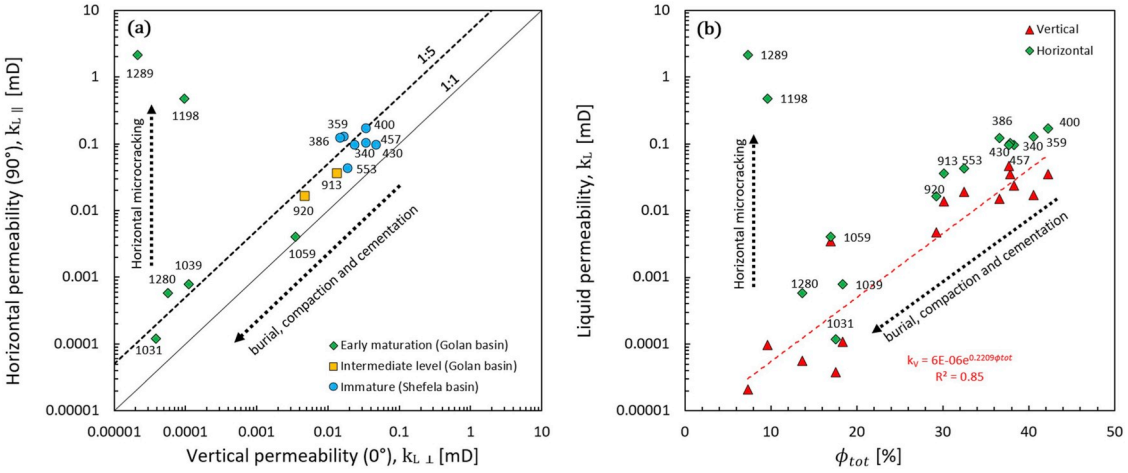

Fig. 9. (a) Horizontal vs. vertical permeability. Ratio of ~1:5 is maintained during burial, compaction and cementation while permeability decreases with depth (direction marked by the dash arrows). However, in the samples taken from 1289 m to 1198 m depths, the permeability of the horizontal samples increases significantly due to the presence of sub-horizontal microcracks (and possibly stylolites) that developed at this stage of burial and maturation. (b) Permeability as a function of porosity. The positive exponential relation of vertical permeability as a function of porosity is presented. The labels of the data points in both graphs represent the depth of each sample.

permeability of the horizontal samples increases significantly. The permeability anisotropy can be demonstrated by the vertical to horizontal permeability ratio (Fig. 7c) and will be further discussed in the discussion section.

It should be noted that, in some cases, the effective porosity measurements underestimate the total porosity (Figs. 7a and 8a). Comparison of the total porosity and effective porosity for nitrogen gas shows that the immature and intermediate stage cores match, while the early maturation cores (samples deeper than 1000 m) deviate significantly from the 1:1 correlation line (Fig. 8a).

Considering dry conditions, the relation of TOC and kerogen density to solid density can be represented using mass and volume balance relationships (Shitrit, 2019; Shitrit et al., 2016; Vernik and Nur, 1992):

$$\rho_s = \frac{\rho_m}{1+\left(\frac{\left(\frac{\rho_m}{\rho_{org}}-1\right)}{100C_{fr}}\right)TOC} \quad . \tag{5}$$

Using the mass balance relationships in equation (4), the Coreval-calculated solid density is presented as a function of TOC (Fig. 8b) and shows a good fit for 1.4 g/cc density of kerogen for the immature and intermediate stages. Nonetheless, the early maturation samples show much lower calculated solid density relative to the TOC value, corresponding to calculated kerogen density of 0.8–1.3 g/cc. These calculations of lower kerogen densities follow from the inaccurate effective porosity measurements, and thus the organic matter density of the early-matured samples suffers a higher degree of uncertainty. In order to address this uncertainty, the calculated total porosity is shown with error bars calculated for the expected range of kerogen densities of 1.2–1.6 g/cc (Figs. 7a and 8a).

Similarly to the previous study of ORC from the Aderet borehole in the Shefela basin carried out by Bisnovat et al. (2015), the vertical to horizontal permeability ratio has an average of ~1:5 (Fig. 9a). This ~1:5 ratio is retained during burial, while the permeability decreases with depth, even in samples with extremely low permeability of tens of nano-Darcy (Fig. 9a). However, in the samples from 1289 m to 1198 m depths, the permeability of the horizontal plugs increases significantly (~1 millidarcy). This will be further discussed in the discussion section.

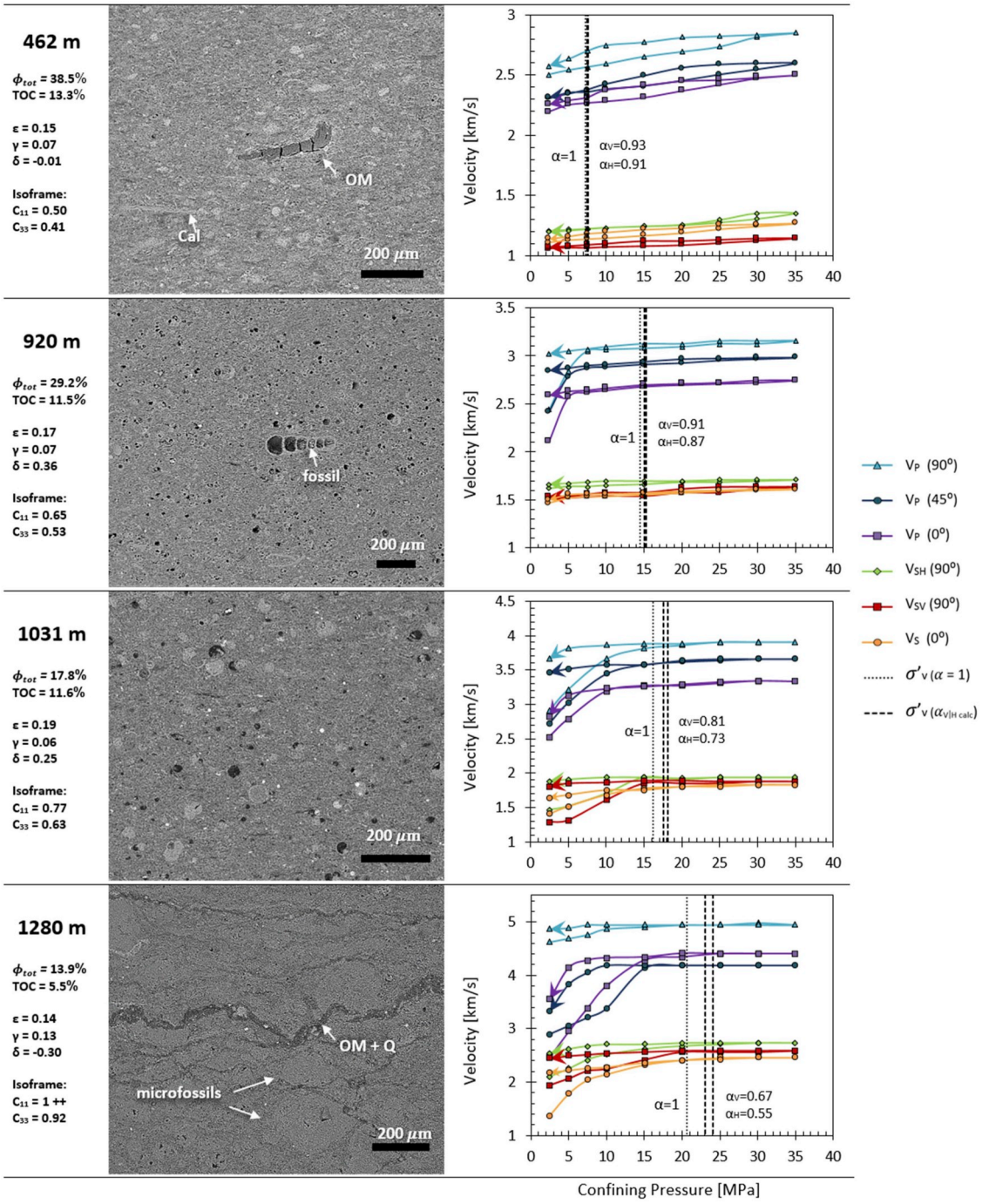

Fig. 10. Four representative measurements of compressional (P) and shear (S) wave velocities as a function of confining pressure (right) and SEM photomicrograph (left) are presented for core samples from depths of: 462 m (the immature stage), 920 m (intermediate section), and 1031 m and 1280 m (early maturation stage). The bedding plane in the SEM images is situated horizontally. Cal stands for calcite, OM for organic matter, and Q for quartz. Three effective stresses were calculated for each depth using Biot's coefficients of: $\boldsymbol{\alpha} = 1$, $\boldsymbol{\alpha_V}$ for the vertical direction, and $\boldsymbol{\alpha_H}$ for the horizontal direction (see calculation in section 3.4).

The vertical permeability as a function of porosity is shown in Fig. 9b. Unlike the horizontal plugs, the permeability of the vertical plugs decrease continuously with depth.

3.2. Ultrasonic velocity measurements

Fig. 10 presents four representative velocity measurements as functions of confining pressures (right) and SEM photomicrographs (left) for the depths of: 462 m (the immature stage), 920 m (intermediate stage), and 1031 m and 1280 m (early maturation stage). Table 4 lists the velocities measured at high pressure of 35 MPa.

Sample 462 m measured velocities as a function of confining pressure displays a quasi-linear increase in velocities with increasing pressure with moderate hysteresis of the three measured P-wave, where the arrow delineates the loading sequence direction from loading to unloading of the confining pressure. This sample exhibits a significant axial strain of ~0.012 or 1.2% axial contraction after being subjected to confining pressure of 35 MPa (Fig. 11). As clearly illustrated in Fig. 11, the deeper the rock has been buried, the more resistant it is to axial contraction when subjected to confining pressure in the lab. This is the

Table 4
Summary of the velocities measured at high pressure (35 MPa). Errors in Vp are ±1–2.2%, and in Vs ±3.2–6.5%, errors decreasing as confining pressure increases.

Depth [m]	Ultrasonic velocities at high pressure (35 MPa) [m/s]					
	V_P (90°)	V_P (45°)	V_P (0°)	V_{SH} (90°)	V_{SV} (90°)	Vs (0°)
400	3053	2850	2623	1397	1337	1322
462	2851	2595	2501	1352	1141	1267
515	3314	3074	2644	1646	1407	1468
553	2884	2952	2543	1598	1578	1364
913	3118	2891	2697	1681	1557	1617
920	3156	2978	2746	1705	1639	1612
1031	3908	3660	3335	1939	1881	1827
1039	4051	3656	3539	2244	2186	2100
1059	4314	4038	3767	2454	2341	2161
1198	4924	4868	4495	2510	2347	2375
1280	4946	4193	4402	2733	2594	2460

result of gravitational compaction and cementation which enhance grain contacts and consequently increases the stiffness of the rock matrix. The axial contraction becomes negligible in samples retrieved from depths greater than 900 m. Due to the observed axial contraction in samples from the shallower depths, length correction were made when needed in calculating the wave velocity.

The estimated vertical *in situ* effective stresses for each sample ($\sigma^{'}$) are delineated by dashed vertical lines in Fig. 10 and are estimated using the following equation:

$$\sigma^{'} = S(v) - \alpha P_P, \tag{6}$$

where $S(v)$ is the total vertical stress, P_p is the pore pressure caused by the fluids in the pore spaces, and α is the Biot effective-stress coefficient. A gradient of 22.6 kPa/m (1 psi/ft.) was used in order to estimate $S(v)$ and the pore pressure (P_p) was estimated based on borehole field measurements provided by the operator (Afek Oil and Gas Ltd). For each depth, three effective stresses were calculated using Biot's coefficients of: $\alpha = 1$, α_V for the vertical direction, and α_H for the horizontal direction (see section 3.4).

When examining sample 920 m, a significant hysteresis in P-wave velocity is observed before the confining pressure reaches the vertical *in situ* effective stress.

The behavior of the velocities of the early-mature samples from 1031 m to 1280 m are different from those of the immature and intermediate stages, as seen in Fig. 10. At the early maturation stage, the hysteresis ends near the estimated vertical effective *in situ* stresses, beyond which hysteresis, as well as velocity variations, are not observed. Velocities are expected to vary at different stages of maturation due to kerogen decomposition, which results in the generation of bitumen and light hydrocarbon molecules as well as in the development of secondary organic porosity and microcracks. Furthermore, the formation of CO_2, H_2S, and organic acids during the first stages of thermal maturation (Allan et al., 2016) may also contribute to the changes in the observed velocities.

It is useful to check the VTI assumption that the order of velocities follows a specific sequence (Martínez and Schmitt, 2013):

$$V_P(90^\circ) > V_P(45^\circ) > V_P(0^\circ) \; and \; V_S(0^\circ) = V_{SV}(90^\circ) \leq V_{SH}(90^\circ) \tag{7}$$

In the present research, Vs (0°) and Vsv (90°) are not always equal. A comparison of these S-wave velocities is presented in Fig. 12 for high (35 MPa, green squares) and low (5 MPa, red circles) confining pressures. It appears that the correlation between Vs (0°) and Vsv (90°) improves with increasing confining pressure.

3.3. Velocity vs. porosity and organic matter

Correlation of compressional and shear wave velocities (or P- and S-impedances) with basic rock properties, such as porosity and kerogen volumetric fraction, can be very useful in geophysical exploration. Fig. 13 presents the measured P- and S-wave velocities at the assumed field effective stress, versus (a) porosity, (b) kerogen volumetric

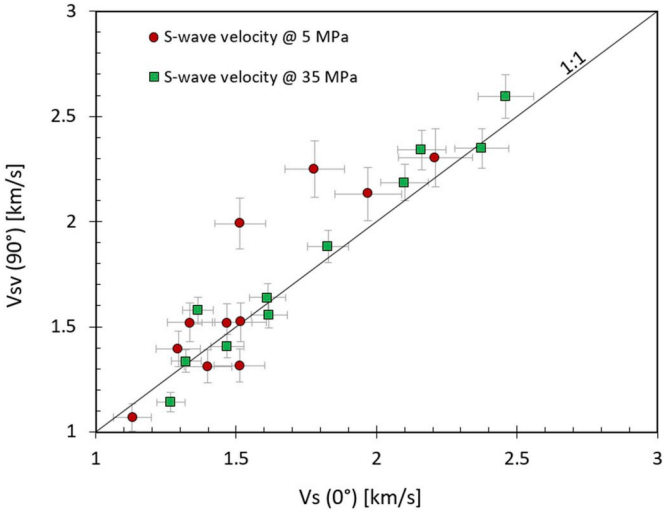

Fig. 12. Comparison of Vsv (90°) and Vs (0°) measured under high and low confining pressures of 35 MPa and 5 MPa, respectively. These S-wave velocities should be equal in a VTI medium. Samples with high S-waves (>1.8 km/s) present a considerable improvement in the correlation with increasing pressure from 5 MPa to 35 MPa. This improvement may be due to the closure of soft porosity and compliant microcracks.

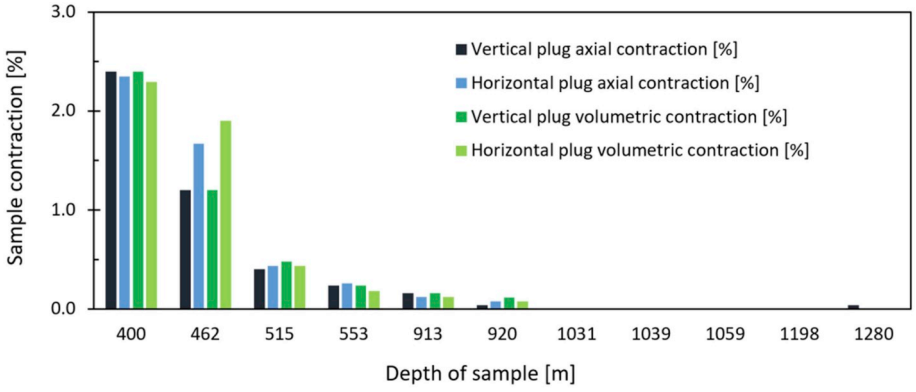

Fig. 11. Axial (normal strain in axial direction) and volumetric contraction of samples for each core measured post-exposure to 35 MPa confining pressure. The deeper the rock was buried, the more it resists contraction. Length correction was made for the shallower depth samples in order to calculate the true wave velocity.

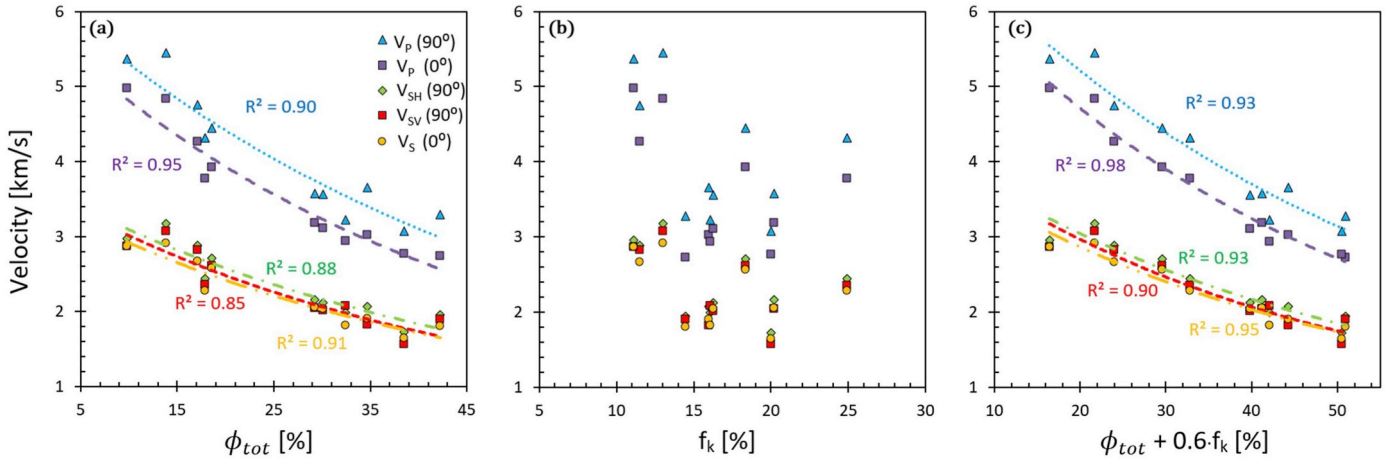

Fig. 13. Compressional and shear wave velocities vs. (a) total porosity, (b) volumetric kerogen content, and (c) the sum of porosity and the factored organic matter volumetric fraction (by 0.6). The velocities were obtained using the assumed *in situ* effective stresses. The velocities decrease with increasing porosity and kerogen fraction, and the exponential correlation becomes optimal (highest possible R^2) when the porosity is modified by adding kerogen content multiplied by factor of 0.6.

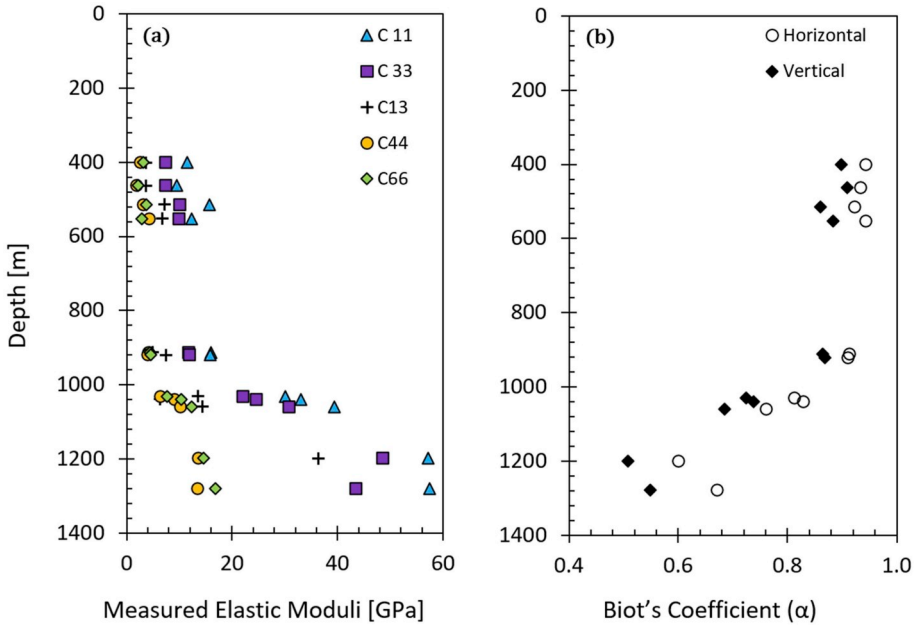

Fig. 14. (a) Elastic moduli vs. depth. Elastic moduli increase significantly below 1000 m due to the chalk transforming into limestone (often referred to as calcareous shale). (b) Biot's coefficient vs. depth (see calculation in section 3.4). Biot's coefficient decreases from ~0.9 at the immature stage to ~0.6 for the early-mature samples. The gap between the horizontal and vertical values represents anisotropic poroelasticity for each depth.

fraction, and (c) the sum of porosity and kerogen volumetric fraction multiplied by a factor of 0.6. Generally, the velocities decrease with increasing porosity and kerogen volume. The velocities show negative exponential correlation with porosity ($R^2 = 0.85 - 0.95$), Fig. 13a. The correlation improves with the sum of porosity and kerogen volume ($R^2 = 0.88 - 0.97$, not presented in this paper), and is optimal (highest possible R^2 value) when the porosity is modified by adding kerogen volumetric fraction multiplied by a scaling factor of 0.6 ($R^2 = 0.90 - 0.98$), Fig. 13c. Nevertheless, our analysis shows that this scaling factor can vary between 0.5 and 1.0 and still provide a reasonable fit with our data. Similar correlation between compressional and shear wave velocities (or P- and S-impedances) and the sum of the porosity and scaled kerogen volume has been reported previously in various organic-rich shale formations (Prasad et al., 2011; Shitrit et al., 2017; Zhao et al., 2018).

Table 5
Physical properties of the rock constituents: density, bulk modulus (K), shear modulus (G), and P-wave modulus (M). Data were selected from Mavko et al. (2019).

Mineral	Density [g/cc]	K [GPa]	G [GPa]	M [GPa]
Calcite	2.71	75	32	118
Quartz	2.65	37.5	44	96
Pyrite	4.93	147.4	132.5	324
Apatite	3.21	86.5	46.6	149
Clay	2	25	9	37
Dolomite	2.87	94.9	45	155
Kerogen	1.4	5	2.5	8.33
Air	0.001291	0.000131	0	0.000131

3.4. Elastic constants and Biot's coefficient

The organic-rich chalks become much stiffer at depths greater than

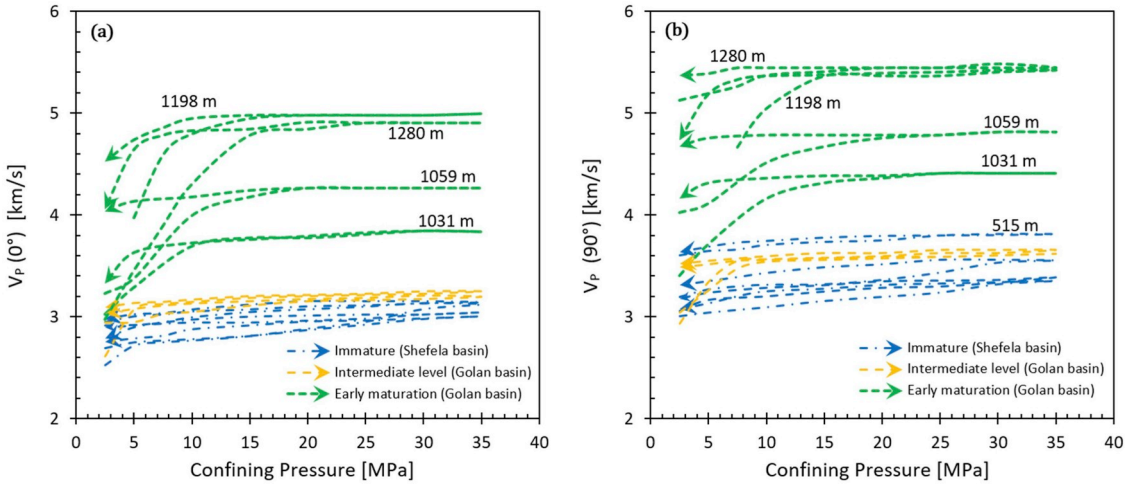

Fig. 15. Compressional wave velocities as a function of confining pressure for all maturation stages. The vertical (a) and horizontal (b) directions are presented. Horizontal velocities (90°) are consistently higher than the vertical one (0°), leading to an elastic anisotropy. Hysteresis of velocities appears only during the early maturation and intermediate stages in both vertical and horizontal directions.

Table 6
Thomsen's parameters calculated for high pressure (35 MPa). Errors in ε and γ are ±4–14%, errors decreasing as confining pressure increases.

Depth [m]	Thomsen parameters at 35 MPa		
	ε	γ	δ
400	0.174	0.056	0.190
462	0.151	0.071	−0.011
515	0.279	0.124	0.507
553	0.160	0.206	0.755
913	0.158	0.033	0.099
920	0.168	0.065	0.355
1031	0.188	0.064	0.248
1039	0.158	0.073	−0.061
1059	0.157	0.147	0.143
1198	0.098	0.057	0.337
1280	0.142	0.128	−0.300

1000 m, as shown by the acoustic velocities and elastic constants (Fig. 14a). Assuming isotropy, Biot's coefficient α (from Equation (5)) can be estimated as:

$$\alpha = 1 - \frac{K_b}{K_m}\,, \tag{8}$$

where K_b is the dry bulk modulus and K_m is the mineral bulk modulus. Here K_m is estimated using XRD analysis, published elastic properties data (Tables 2 and 5), and Voigt average. K_b is calculated using elasticity relationships $\left[K_b = \rho_b\left(V_P^2 - \frac{4}{3}V_S^2\right.\right]$. The variation of α with depth is shown in Fig. 14b. The velocities measured in the vertical and horizontal directions allowed us to indirectly estimate the Biot's coefficient for these directions and to better estimate the variations in the *in situ* effective stresses (see Fig. 10). A similar approach for describing α in the orthogonal directions based on Equation (7) was used by Prasad et al. (2011).

In the immature cores from the Shefela basin (depths 400–553 m), the average value of α is = 0.9, similar to findings from a previous study of ORC from the Shefela basin (Shitrit et al., 2016). α decreases significantly to ~0.6, however, in the early-mature samples (depths 900–1280 m), which is a more common value for stiffer shale rocks (He et al., 2016; Ma and Zoback, 2015). The gap between the horizontal and vertical α values represents the anisotropy for each core (Fig. 14b).

3.5. Pressure sensitivity of the ultrasonic waves velocity

We obtained consistently higher P-wave velocities in the horizontal direction than the vertical one (Fig. 15), indicating weak elastic anisotropy of the organic-rich chalk. The calculated Thomsen's anisotropy parameters for high confining pressures (35 MPa) are displayed in Table 6. The variation of Thomsen's ε and γ parameters with increasing confining pressure from 0 to 35 MPa is shown in Fig. 16. The immature and intermediate samples show no significant changes whereas some of the early-mature samples do show a significant change in Thomsen's ε and γ parameters at low confining pressures.

Thomsen's P-wave anisotropy parameter ε as a function of (a) total porosity, (b) kerogen volumetric fraction, and (c) the sum of porosity and kerogen volumetric fraction is illustrated in Fig. 17. The dark colors represent the anisotropy measured at the calculated, field effective pressure (see Fig. 10) and the light colors represent the anisotropy measured at high pressure of 35 MPa. The P-wave anisotropy generally decreases with loss of porosity (and increased burial depth), and increases with kerogen content. The correlation of ε against the sum of the total porosity and kerogen volumetric fraction becomes better and can be beneficial for many practical cases (Zhao et al., 2018) (Fig. 17c). The deviations from this general trend are discussed below.

4. Discussion

4.1. Sources of anisotropy as inferred from SEM micrographs

Calcite is the dominant mineral constituent in this set of ORC samples, while clay minerals are scarce and occupy only 0–3.5%. It appears, therefore, that clays are not a dominant factor affecting the observed anisotropy. Preferred orientation parallel to bedding of elements such as organic matter (kerogen), microcracks, micro fossils, and minerals, are detected using SEM photomicrographs (Figs. 10 and 18). Lenticular kerogen shapes are common at almost all stages of burial and seem to be consistently aligned with bedding plane direction. This preferred orientation of the organic matter can strongly affect VTI behavior. We find evidence for initial generation of pressure dissolution structures from depth of ~1050 m (Fig. 18) including complexes of organic matter adjacent to stylolite structures (Fig. 10 botton and Fig. 18b). Pressure dissolutions usually take place between calcite and silica or clay, and as a result more calcite dissolves and is available for re-utilization as pore-filling cementation (Fabricius, 2003). Indeed, EDS analysis confirms the presence of small amounts of quartz and kerogen adjacent to stylolite

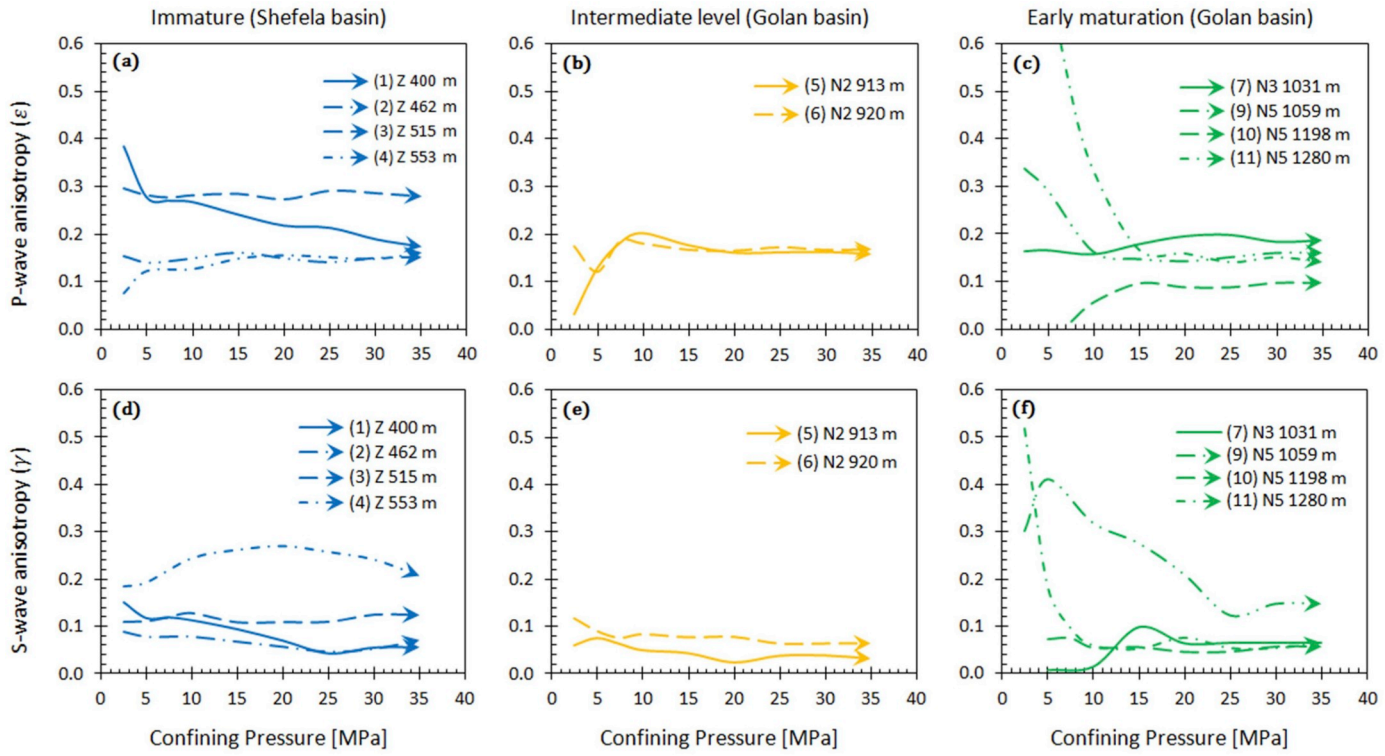

Fig. 16. The calculated Thomsen's P- and S-wave anisotropy parameters vs. confining pressure, measured while raising the pressures from 0 to 35 MPa. For the immature and intermediate levels of maturation, the anisotropy values are relatively constant (left and middle figures), yet in some of the early-matured cores, the anisotropy is very sensitive to pressures changes (right figures).

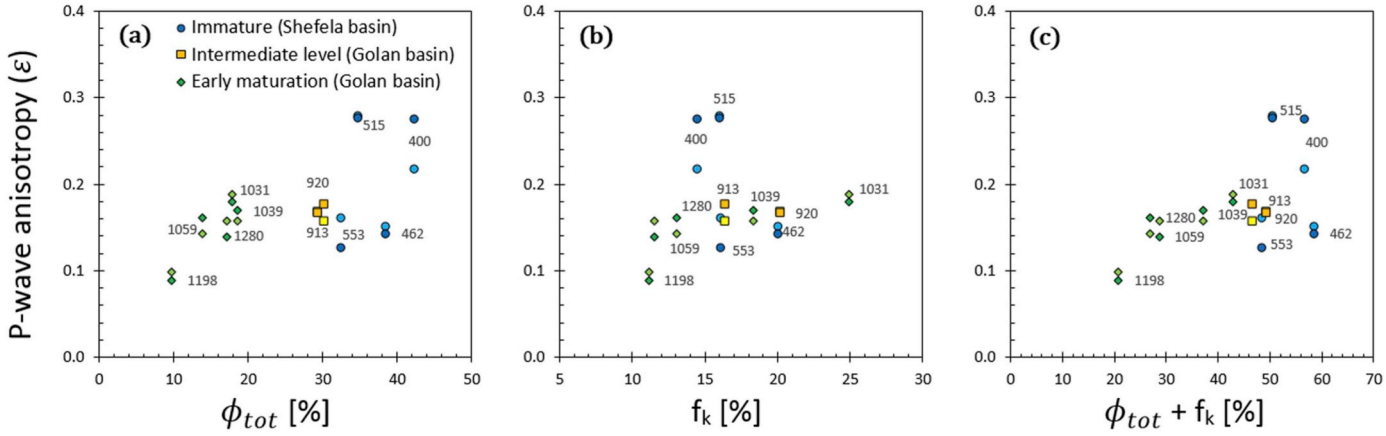

Fig. 17. Thomsen's P-wave anisotropy parameter ε vs. (a) porosity, (b) volumetric kerogen content, and (c) the sum of porosity and volumetric kerogen content. The dark colors represent the anisotropy measured at the assumed effective stress in the field and the light colors represent the anisotropy measured at high pressure of 35 MPa. (For interpretation of the references to color in this figure legend, the reader is referred to the Web version of this article.)

structures. Pressure dissolutions are also accompanied by decreasing porosity due to pore-filling cementation, and lead to the transformation of the ORC into limestone.

4.2. Anisotropy evolution through maturation stages

ORC sediments are deposited under deep marine conditions where shells of micro-organisms and organic matter accumulate on the sea floor as suspension and are buried. The deeper these sediments are buried, the more they are subjected to increasing pressure and temperature, which also affect the anisotropy, as discussed below.

4.3. Immature stage, T_{MAX} of 403–415°C and 340–553 m

This stage follows primary chalk generation, typically between 200 and 300 m depth, where contact cementation between shells occurs, transforming the ooze into chalk. At depth interval between 340 and 553 m, the chalk is still soft and characterized by high porosity of 30–40% and permeability of 0.14–0.015 mD. The porosity decreases significantly with burial depth at this stage, and the permeability ratio increases (Fig. 7). The increase in permeability ratio represents a decrease in permeability anisotropy. Since contact cementation between particles does not necessarily develop in a specific direction, it is likely that the rock matrix will become more isotropic at this stage.

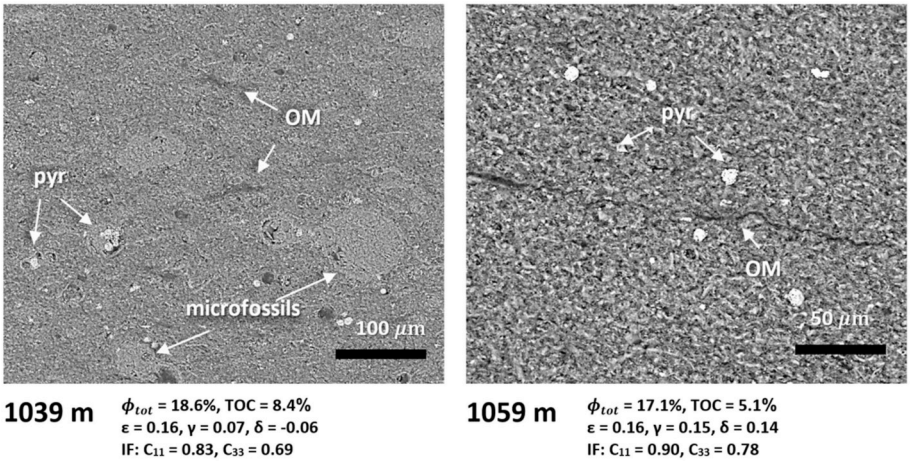

Fig. 18. SEM images of the early-mature samples from the depth of 1039 m (left) and 1059 m (right). OM stands for organic matter and pyr for framboidal pyrite. Initial generation of pressure dissolution structure (stylolite) accompanied by organic matter concentration is identified in the sample from the depth of 1059 m (right).

4.4. *Intermediate stage, T_{MAX} of 423–424°C and 912–920 m*

At this stage the porosity remains a little under 30%, similar to the porosity of the deepest cores from the Shefela basin (Figs. 6a and 7a). SEM photomicrographs indicate the preservation of intra-microfossil porosity (Fig. 10, sample 920 m). The preservation of chalk intra-fossils porosity at this stage of diagenesis has been previously observed in non-organic chalks (Fabricius, 2003; Grützner and Mienert, 1999) and presented in Fig. 6a [Trend of the North Sea chalk from Kroenke et al. (1991)]. A possible explanation might be compaction and contact cementation between particles accompanied by calcite-calcite recrystallization, which increase the rock frame strength and prevent intra-fossils pores from collapsing. At this stage, the pore volume remains relatively constant since only extant calcite is involved in the process and no external source of dissolved calcite is available for intra-porous cementation. For mechanical compaction to proceed, the effective stress must overcome the strength of contact cementation, either by deeper burial or by drawdown of pore pressure (Fabricius, 2003).

A significant hysteresis in P-wave velocity is observed in the intermediate samples from 913 m to 920 m (Figs. 10 and 15), which stops before the confining pressure reaches the estimated vertical *in situ* effective stress. This may suggest the development of soft porosity, such as secondary organic porosity, microcracks, or sub-microcracks, initiating at the depth of ~900 m as a result of entering the oil window stage and primary expulsion. The slight increase in the velocities at confining pressures greater than the *in situ* effective stresses may reflect elastic deformation related to soft porosity compression and increased contact between the grain particles.

4.5. *The early maturation stage, T_{MAX} of 428–434°C and 1031–1289 m*

The early maturation stage is characterized by the following: high bitumen content, low porosity, low vertical permeability, decreasing Biot's coefficient, high velocities, and high elastic constants. At this stage the core plug samples are well resistant to axial contraction during the velocity measurements under a confining pressure of 35 MPa (Fig. 11). This might be the result of pressure-induced compaction, pressure dissolution, and pore-filling cementation (e.g. intra-fossils) resulting in reduced porosity. The maturation of the organic matter may also contribute to the rock stiffness. Furthermore, at this stage, the Coreval porosity measurements underestimate the total porosity (Figs. 7a and 8a). Comparison between the total porosity and the measured (effective for nitrogen gas) porosity shows that the immature and intermediate stage cores match, while the early maturation cores (all samples deeper than 1000 m) deviate significantly from the 1:1 correlation line (Fig. 8a). This gap appears to be the result of thermal maturation - where the bitumen generated during early maturation stage clogs pore throats and prevents the nitrogen gas from accessing the entire pore-space during the measurements. This is confirmed by density and NMR well-logs in these wells.

Both the porosity and the permeability ratio decreases significantly with burial depth at this stage (Fig. 7a and c). The decrease in the permeability ratio represents an increase in permeability anisotropy, which demonstrates a reverse trend from the immature stage samples. Initial generation of pressure dissolution structures is illustrated in the SEM photomicrograph of sample 1059 m (Fig. 18 right) and well-developed stylolite structures together with preferred orientation of organic matter veins along these structures is illustrated in the SEM photomicrograph of sample 1280 m (Fig. 10 bottom). These structures developed during the early thermal maturation stage simultaneously with the diagenetic chalk-limestone transformation stage (between 1000 m–1300 m) and may enhance anisotropy for petrophysical properties.

The velocity sensitivity of the early-matured samples at low effective stresses (Fig. 10 bottom and Fig. 15), indicates the presence of soft porosity. This sensitivity was not observed in the immature samples suggesting it might be the result of the early maturation and entering the oil window stage. In the samples from 1289 m to 1198 m depths, the permeability of the horizontal plugs increases significantly up to ~1 millidarcy (Fig. 9b). This is most likely the result of preferred orientation for gas flow in sub-horizontal microcracks parallel to pressure dissolution structures in these samples. This observation suggests that the sub-horizontal microcracks formed at this stage of maturation are characterized by a permeability of ~1 millidarcy and may represent an upper constraint for petrophysical models of ORCs.

At the early maturation stage, the P-wave anisotropy decreases with porosity loss and burial depth and increases with kerogen content (Fig. 17). Although it appears that anisotropy generally decreases with depth, increased anisotropy from ε equals 0.13 to 0.18, seems to be associated with a limited range - from the deepest immature sample (553 m), through the intermediate level samples, to the shallowest early-matured core (1031 m, Fig. 17). This may be the result of the emergence of soft porosity at this stage of entering the oil window, possibly generated by primary expulsion, secondary organic porosity development, and generation of microcracks.

Considering the general decrease of velocity anisotropy with diagenesis and the development of soft porosity with the progress of

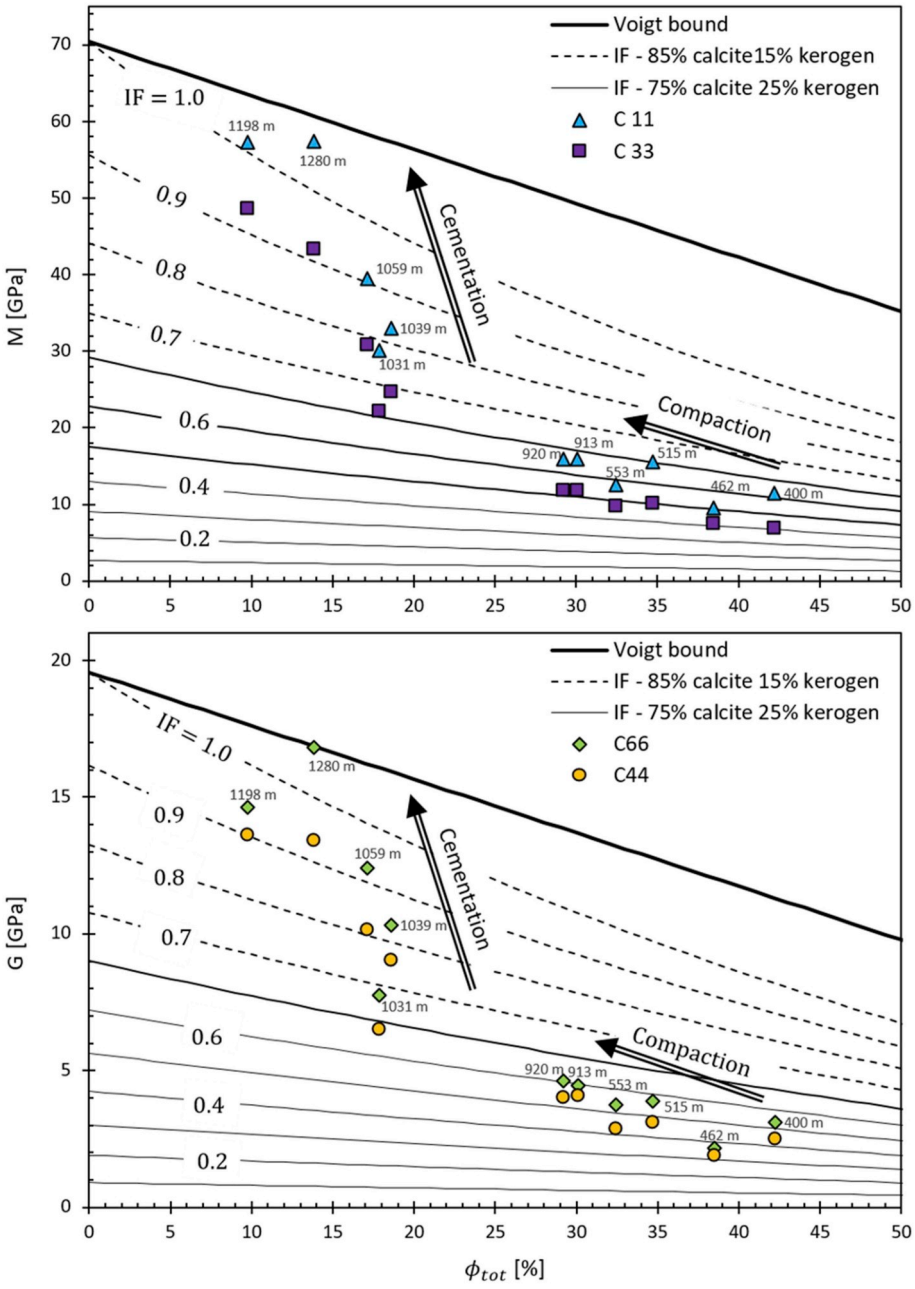

Fig. 19. P-wave modulus (top panel) and shear modulus (lower panel) vs. porosity displayed over the Iso-Frame (IF) model for organic-rich chalk. The Iso-Frame model is an effective-medium model based on modified upper Hashin-Shtrikman (MUHS) bounds of Nur et al. (1995) as presented by Fabricius (2003). Iso-Frame values represent how much of the solid phases are embedded in the supporting frame, and how much is in suspension. Whereas a moderate trend of increasing IF with porosity lost in the immature and intermediate stages is observed (arrow marked 'compaction'), the early-mature stage presents a sharp slope of increasing IF and particularly high IF value of over one, reaching the upper Voigt bound (arrow marked 'cementation'). Values of IF are summarized in Table 7 and discussed in section 4.3.

maturation – in addition to the sub-horizontal accumulation of organic matter alongside stylolites – it is reasonable to assume that further maturation *in situ* may enhance P-wave velocity anisotropy. This might be the case especially at "sweet spots" with high internal pore pressures due to the generation and accumulation of light hydrocarbon fluids resulting in low effective stresses. This relation between the velocity anisotropy and light hydrocarbon fluids may prove to be useful in seismic exploration.

4.6. Analysis of conceptual rock physics models

The Iso Frame (IF) model (Fabricius, 2003) is an effective medium model in which the IF Value quantifies, on a scale from 0 to 1, the amount of solids required to take part of the load-supporting frame of the rock. The rest of the solids are assumed to be suspended in the pore-fluid and do not to take part in supporting the rock frame. This model helps explain how the properties of the ORCs change during diagenesis, as cementation develops and porosity decreases. Using the velocity measurements in the vertical and horizontal directions, combined with the IF method, we can estimate how much of the solid phases (mixture of minerals and kerogen) are required to be embedded in the supporting frame in these orthogonal directions. Fig. 19 presents the P- and S-wave moduli vs. porosity above the IF model for organic-rich chalk and the IF values are summarized in Table 7.

The moderate trend of increasing IF with porosity lost in the shallower immature and intermediate stages samples possibly reflects a mechanical compaction and the generation of contact grain cementation between calcite particles (Fig. 19, arrow marked 'compaction'). This hypothesis fits the observation of decreasing porosity, permeability and permeability anisotropy at this stage (Fig. 7). Nonetheless, at the early maturation stage, a sharp slope of increasing IF is observed. This sharp slope demonstrates the generation of calcite pore-filling cementation,

Table 7
Estimated Iso-Frame (IF) values are presented. *The immature and intermediate stages are represented by Voigt-Ross-Hill (VRH) solids mixture of 75% calcite and 25% OM (IF range of 0–0.7), while the early maturation stage** is represented by VRH solids mixture of 85% calcite and 15% OM (IF range of 0.6–1; see Fig. 19).

Depth [m]	IF C11 (90°)	IF C33 (0°)	IF C44 (0°)	IF C66 (90°)
400*	0.62	0.41	0.44	0.53
462*	0.50	0.41	0.33	0.36
515*	0.70	0.50	0.47	0.57
553*	0.56	0.48	0.43	0.54
913*	0.66	0.53	0.56	0.59
920*	0.65	0.53	0.54	0.68
1031**	0.77	0.63	0.60	0.68
1039**	0.83	0.69	0.76	0.84
1059**	0.90	0.78	0.81	0.93
1198**	1+	0.93	0.94	0.90
1280**	1++	0.92	Voigt	0.94

when calcite being available for precipitation due to pressure dissolution occurring at this stage of diagenesis (Fig. 19, arrow marked 'cementation'). The newly precipitated pore-filling calcite, demonstrated by the SEM images in Fig. 10 (bottom) and Fig. 18 (left), fills up the intra-fossils porosity and connects the original sediment grains, thereby forming a much stiffer rock frame.

The elastic anisotropy of the ORC can also be demonstrated by the difference between the IF values for the elastic moduli C_{11} and C_{33} as well as C_{44} and C_{66} (for P- and S-wave impedances, respectively). It is noticeable how, in general, the IF anisotropy consistently increases with cementation developed at the early maturation stage. At this stage, the horizontal P- and S-impedances (C_{11} and C_{66}) showed extremely high IF value of over one for the deepest core samples, and even reaches the upper Voigt bound. This indicates that in the horizontal direction, at this stage of diagenesis, the rock frame is exclusively supported by all the available solid phases and none of the solids are in suspension. Based on IF analysis and the visual observation (SEM) of horizontal orientation of organic matter along pressure dissolution structures at the early-mature stage (Fig. 10 bottom), we suggest that induced pore pressure due to HC generation and consequent decrease of the effective stress, may affect the vertical direction more than the horizontal that is exclusively supported by solids phases and therefore less sensitive. This is also supported by the Biot's coefficient analysis (Fig. 14b) showing a lower α value for the horizontal direction. As suggested earlier, this may enhance velocity anisotropy at sweet spot locations in carbonate shale, and perhaps be utilized to develop remote detection techniques for hydrocarbon exploration.

5. Summary and conclusions

Laboratory measurements of organic-rich carbonate cores from depth ranges of 340–1289 m were used to investigate the ultrasonic wave velocity and permeability anisotropies. At these depths, the rock properties change significantly due to both (1) burial diagenesis - from the soft chalk to the chalk-limestone diagenetic sequence and (2) the thermal maturation of the organic matter – converting from the immature (T_{MAX} of 403–415°C) to the early maturation stage (T_{MAX} of 428–434°C), when entering the oil window stage. The thermal maturation was evaluated separately by Rosenberg et al. (in prep.).

We propose that ORC diagenesis is to some extent comparable to the diagenetic stages of non-organic chalk, and that an effective medium model such as the Iso-Frame can be employed to represent ORC diagenesis. Nevertheless, the characteristics and distribution of the organic matter, which change significantly throughout burial and thermal maturation, strongly affect velocity and permeability anisotropies. These changes must therefore be included when the physical behavior of ORC is thoroughly investigated.

Velocity hysteresis during pressurization and depressurization shows that soft porosity plays a significant role in the early-matured samples (from the Golan basin), while it is absent in the immature core samples (from the Shefela basin).

Beginning at depth of 1000 m, elongated horizontal pressure dissolution stylolite structures and preferred orientation of organic matter veins along these stylolite structures were identified (Fig. 10 bottom and Fig. 18). At this stage, the intra-fossils porosity is almost fully cemented.

The Iso-Frame effective-medium model was used to exemplify how much of the solid phases were embedded in the supporting frame of the ORC, in the horizontal and vertical direction, for each stage of diagenesis. At the deepest core extracted from 1280 m depth (from the early maturation stage), extremely high IF values appeared in the horizontal direction, which indicates that the rock matrix is exclusively supported by all the available solid phases in that direction and that none of the solid phases are in suspension. This stage of burial might also represent the transformation of ORC into organic-rich limestone (or organic-rich calcareous shales) simultaneously with early maturation of the organic matter.

Based on our observations we hypothesize that at sweet spots locations in unconventional organic-rich carbonate reservoirs, changes in the effective stresses caused by light hydrocarbon pore pressure generation during further maturation, may affect the vertical direction rather than the horizontal one. This may cause variations in wave velocities, enhance velocity anisotropy, and aid in seismic exploration for carbonate unconventional self-sourced reservoirs.

Author contributions section

Yair Gordin: Conceptualization, Methodology, Investigation, Writing - original draft. Yossef H. Hatzor: Supervision, Writing - review & editing, Validation, Resources. Harold J. Vinegar: Supervision, Writing - review & editing, Validation, Resources.

Acknowledgments

This research was funded by Afek Oil and Gas Ltd. We would like to thank Dr. Yuval Bartov of Afek Oil and Gas Ltd. for providing core samples for this study and for allowing us to cite their TOC and T_{MAX} values as shown in Table 1. We thank the Israel Ministry of National Infrastructures, Energy, and Water Resources for supporting this research through a special Graduate Studies Fellowship in Petroleum Sciences, [contract no. 217-01-039]. The first author gratefully acknowledges support from the Robin and Harold Vinegar Graduate Fellowship fund. We thank Prof. Shimon Feinstein, Prof. Chaim Benjamini, and Dr. Yoav Rosenberg for their help and for fruitful discussions. Dr. Omri Shitrit is thanked for being a partner in many fruitful discussions. We would like to express gratitude to Leonardo Freitas for his great assistance in sample preparation and to Edna Danon for Rockeval measurements. Finally, we wish to thank the three anonymous reviewers for their critical review and constructive comments.

Appendix A. Supplementary data

Supplementary data to this article can be found online at https://doi.org/10.1016/j.petrol.2020.106946.

References

Allan, A.M., Clark, A.C., Vanorio, T., Kanitpanyacharoen, W., Wenk, H.-R., 2016. On the evolution of the elastic properties of organic-rich shale upon pyrolysis-induced thermal maturation. Geophysics 81, D263–D281. https://doi.org/10.1190/geo2015-0514.1.

Allan, A.M., Kanitpanyacharoen, W., Vanorio, T., 2015. A multiscale methodology for the analysis of velocity anisotropy in organic-rich shale. Geophysics 80, C73–C88. https://doi.org/10.1190/geo2014-0192.1.

Allan, A.M., Vanorio, T., Dahl, J.E.P., 2014. Pyrolysis-induced P-wave velocity anisotropy in organic-rich shales. Geophysics 79, D41–D53. https://doi.org/10.1190/geo2013-0254.1.

Bisnovat, K., Hatzor, Y.H., Vinegar, H.J., Nguyen, S.V., Palchik, V., Feinstein, S., 2015. Mechanical and petrophysical behavior of organic-rich chalk from the Judea Plains, Israel. Mar. Pet. Geol. 64, 152–164. https://doi.org/10.1016/j.marpetgeo.2015.02.044.

Burg, A., Gersman, R., 2016. Hydrogeology and geochemistry of low-permeability oil-shales – case study from HaShfela sub-basin. Israel. J. Hydrol. 540, 1105–1121. https://doi.org/10.1016/j.jhydrol.2016.07.026.

Carcione, J.M., 2007. Wave Fields in Real media: Wave Propagation in Anisotropic, Anelastic, Porous and Electromagnetic Media, 38. Elsevier.

Chichinina, T., 2017. Physical constraints on C 13 for transversely isotropic shales and their applications. Geophysics 82, WA105–WA118. https://doi.org/10.1190/GEO2016-0656.1.

Dewhurst, D.N., Siggins, A.F., Sarout, J., Raven, M.D., Nordgård-Bolås, H.M., 2011. Geomechanical and ultrasonic characterization of a Norwegian Sea shale. Geophysics 76, WA101. https://doi.org/10.1190/1.3569599.

Eyal, Y., Reches, Z., 1983. Tectonic analysis of the Dead Sea Rift Region since the Late-Cretaceous based on mesostructures. Tectonics 2, 167–185. https://doi.org/10.1029/TC002i002p00167.

Fabricius, I.L., 2003. How burial diagenesis of chalk sediments controls sonic velocity and porosity. Am. Assoc. Petrol. Geol. Bull. 87, 1755–1778. https://doi.org/10.1306/06230301113.

Fabricius, I.L., Høier, C., Japsen, P., Korsbech, U., 2007a. Modelling elastic properties of impure chalk from South Arne field, North Sea. Geophys. Prospect. 55, 487–506. https://doi.org/10.1111/j.1365-2478.2007.00613.x.

Fabricius, I.L., Rogen, B., Gommesen, L., 2007b. How depositional texture and diagenesis control petrophysical and elastic properties of samples from five North Sea chalk fields. Pet. Geosci. 13, 81–95. https://doi.org/10.1144/1354-079306-707.

Flexer, A., 1971. Late Cretaceous paleogeography of northern Israel and its significance for the Levant geology. Palaeogeogr. Palaeoclimatol. Palaeoecol. 10, 293–316. https://doi.org/10.1016/0031-0182(71)90053-8.

Freund, A.R., Garfunkel, Z., Zak, I., Goldberg, M., Weissbrod, T., Derin, B., Bender, F., Wellings, E., Girdler, R.W., 1970. The shear along the Dead Sea rift. Philos. Trans. R. Soc. London A Math. Phys. Eng. Sci.

Freund, R., Zak, I., Garfunkel, Z., 1968. Age and rate of the sinistral movement along the dead sea rift [6]. Nature. https://doi.org/10.1038/220253a0.

Gardosh, M.a., Tannenbaum, E., 2014. The petroleum systems of Israel. In: AAPG Search and Discovery Article, pp. 179–216. https://doi.org/10.1306/13431857M106298.

Grützner, J., Mienert, J., 1999. Physical property changes as a monitor of pelagic carbonate diagenesis: an empirically derived diagenetic model for Atlantic Ocean basins. Am. Assoc. Petrol. Geol. Bull. 83, 1485–1501.

Gvirtzman, G., Almogi-Labin, A., Moshkovitz, S., Lewy, Z., Honigstein, A., Reiss, Z., 1989. Upper Cretaceous high-resolution multiple stratigraphy, northern margin of the Arabian platform, central Israel. Cretac. Res. 10, 107–135. https://doi.org/10.1016/0195-6671(89)90001-3.

Hashin, Z., Shtrikman, S., 1963. A variational approach to the theory of the elastic behaviour of multiphase materials. J. Mech. Phys. Solids 11, 127–140. https://doi.org/10.1016/0022-5096(63)90060-7.

He, J., Rui, Z., Ling, K., 2016. A new method to determine Biot's coefficients of Bakken samples. J. Nat. Gas Sci. Eng. 35, 259–264. https://doi.org/10.1016/j.jngse.2016.08.061.

Horne, S.A., 2013. A statistical review of mudrock elastic anisotropy. Geophys. Prospect. 61, 817–826. https://doi.org/10.1111/1365-2478.12036.

Kaviani, A., Hofstetter, R., Rümpker, G., Weber, M., 2013. Investigation of seismic anisotropy beneath the Dead Sea fault using dense networks of broadband stations. J. Geophys. Res. Solid Earth 118, 3476–3491. https://doi.org/10.1002/jgrb.50250.

Koren, Z., Ravve, I., Levy, R., 2009. Effective model for HTI/VTI layered media. In: SEG Annual Meeting, pp. 286–290.

Kroenke, L.W., Berger, W.H., Janecek, T.R., et al., 1991. Proceedings of the ocean drilling program, initial reports 130, Ontong Java plateau. Ocean drilling program. https://doi.org/10.1142/9781848161269_0001.

Kutuzov, I., 2017. Study of the Early Stage Immature Oil Produced from the Israeli Oil Shale. MSc Thesis. Ben-Gurion University of the Negev, Be'er Sheva, Israel.

Levitte, D., Greitzer, Y., 2005. Geothermal update report from Israel 2005, Proceedings World Geothermal Congress.

Lo, T.W., Coyner, K.B., Toksoz, M.N., 1986. Experimental determination of elastic anisotropy of Berea sandstone, Chicopee shale, and Chelmsford granite. Geophysics 51, 164–171. https://doi.org/10.1190/1.1442029.

Ma, X., Zoback, M.D., 2015. Experimental study of the Biot coefficient of Bakken cores. Am. Geophys. Union Fall Meet 2015. Abstr. id. MR43A-03.

Marco, S., Rockwell, T.K., Heimann, A., Frieslander, U., Agnon, A., 2005. Late Holocene activity of the Dead Sea Transform revealed in 3D palaeoseismic trenches on the Jordan Gorge segment. Earth Planet. Sci. Lett. 234, 189–205. https://doi.org/10.1016/j.epsl.2005.01.017.

Martínez, J.M., Schmitt, D.R., 2013. Anisotropic elastic moduli of carbonates and evaporites from the Weyburn-Midale reservoir and seal rocks. Geophys. Prospect. 61, 363–379. https://doi.org/10.1111/1365-2478.12032.

Mavko, G., Mukerji, T., Dvorkin, J., 2019. The Rock Physics Handbook. Cambridge University Press.

Meiler, M., Reshef, M., Shulman, H., 2011. Seismic depth-domain stratigraphic classification of the golan Heights, central Dead Sea fault. Tectonophysics 510, 354–369. https://doi.org/10.1016/j.tecto.2011.08.007.

Meilijson, A., Ashckenazi-Polivoda, S., Ron-Yankovich, L., Illner, P., Alsenz, H., Speijer, R.P., Almogi-Labin, A., Feinstein, S., Berner, Z., Püttmann, W., Abramovich, S., 2014. Chronostratigraphy of the Upper Cretaceous high productivity sequence of the southern Tethys, Israel. Cretac. Res. 50, 187–213. https://doi.org/10.1016/j.cretres.2014.04.006.

Meléndez-Martínez, J., Schmitt, D.R., 2016. A comparative study of the anisotropic dynamic and static elastic moduli of unconventional reservoir shales: implication for geomechanical investigations. Geophysics 81, D245–D261. https://doi.org/10.1190/GEO2015-0427.1.

Mimran, Y., Druckman, Y., Moshkovitz, S., Grossowicz, L.P., Sneh, A., 1985. The stratigraphy of the Mount Scopus Group in the northern Golan and its structural implications. Isr. J. Earth Sci. 34, 229–239.

Minster, T., 2009. Oil Shale Deposits in Israel., Geological Survey Report. GSI/18/2009.

Minster, T., Nathan, Y., Raveh, A., 1992. Carbon and sulfur relationships in marine Senonian organic-rich, iron-poor sediments from Israel — a case study. Chem. Geol. 97, 145–161. https://doi.org/10.1016/0009-2541(92)90141-Q.

Mor, D., Michelson, H., Druckman, Y., Mimran, Y., Heiman, A., Goldberg, M., Sneh, A., 1997. Notes on the Geology of the Golan Heights. Israel, Geological Survey Report. GSI/15/97.

Nur, A.M., Mavko, G., Dvorkin, J., Gal, D., 1995. Critical porosity: the key to relating physical properties to porosity in rocks. In: SEG Technical Program Expanded Abstracts 1995, pp. 878–881. https://doi.org/10.1190/1.1887540.

Pervukhina, M., Rasolofosaon, P.N.J., 2017. Compaction trend versus seismic anisotropy in shaly formations. Geophys. Prospect. 65, 1351–1365. https://doi.org/10.1111/1365-2478.12486.

Prasad, M., Mba, K., Sadler, T., Batzle, M., 2011. Maturity and impedance analysis of organic-rich shales. SPE Reserv. Eval. Eng. 14, 14–16. https://doi.org/10.2118/123531-PA.

Røgen, B., 2002. PhD Thesis: North Sea Chalk - Textural, Petrophysical, and Acoustic Properties. Technical University of Denmark (DTU).

Rosenberg, O.Y., Reznik, J.I., Vinegar, H.J., Feinstein. S., Bartov Y., Comparing natural and artificial thermal maturation of a Type II-S source rock, Late Cretaceous, Israel. In preparation.

Sarout, J., Esteban, L., Piane, C.D., Maney, B., Dewhurst, D.N., 2014. Elastic anisotropy of Opalinus Clay under variable saturation and triaxial stress. Geophys. J. Int. 198, 1662–1682. https://doi.org/10.1093/gji/ggu231.

Sarout, J., Molez, L., Guéguen, Y., Hoteit, N., 2007. Shale dynamic properties and anisotropy under triaxial loading: experimental and theoretical investigations. Phys. Chem. Earth 32, 896–906. https://doi.org/10.1016/j.pce.2006.01.007.

Sayers, C.M., 2013. The effect of kerogen on the elastic anisotropy of organic-rich shales. Geophysics 78, D65–D74. https://doi.org/10.1190/GEO2012-0309.1.

Shalev, E., Lyakhovsky, V., Weinstein, Y., Ben-Avraham, Z., 2013. The thermal structure of Israel and the Dead Sea fault. Tectonophysics 602, 69–77. https://doi.org/10.1016/j.tecto.2012.09.011.

Shitrit, O., 2019. PhD Thesis: Relationships between Physical Properties and Maturation of Organic - Rich Chalk in Two Basins in Israel: Laboratory and Field Measurements. Ben-Gurion University of the Negev.

Shitrit, O., Hatzor, Y.H., Feinstein, S., Palchik, V., Vinegar, H.J., 2016. Effect of kerogen on rock physics of immature organic-rich chalks. Mar. Pet. Geol. 73, 392–404. https://doi.org/10.1016/j.marpetgeo.2016.03.023.

Shitrit, O., Hatzor, Y.H., Feinstein, S., Vinegar, H.J., 2017. Acoustic and petrophysical evolution of organic-rich chalk following maturation induced by unconfined pyrolysis. Rock Mech. Rock Eng. 50, 1–19. https://doi.org/10.1007/s00603-017-1325-9.

Shulman, H., Reshef, M., Ben-Avraham, Z., 2004. The structure of the Golan Heights and its tectonic linkage to the Dead Sea Transform and the Palniyrides folding. Isr. J. Earth Sci. 53, 225–237. https://doi.org/10.1560/MWVC-CGPU-65KU-FFPY.

Spiro, B., 1980. Geochemistry and Mineralogy of Bituminous Rocks in Israel. Unpublished PhD. Hebr. Univ. Jerusalem, Isr.

Thomsen, L., 1986. Weak elastic anisotropy. Geophysics 51, 1954–1966. https://doi.org/10.1190/1.1442051.

Tsvankin, I., 1997. Reflection moveout and parameter estimation for horizontal transverse isotropy. Geophysics 62, 614. https://doi.org/10.1190/1.1444170.

Vernik, L., Landis, C., 1996. Elastic anisotropy of source rocks: implications for hydrocarbon generation and primary migration. Am. Assoc. Petrol. Geol. Bull. 80, 531–544. https://doi.org/10.1306/64ED8836-1724-11D7-8645000102C1865D.

Vernik, L., Nur, A., 1992. Ultrasonic velocity and anisotropy of hydrocarbon source rocks. Geophysics 57, 727–735. https://doi.org/10.1190/1.1443286.

Yan, F., Han, D.H., Yao, Q., 2016. Physical constraints on c 13 and δ for transversely isotropic hydrocarbon source rocks. Geophys. Prospect. 64, 1524–1536. https://doi.org/10.1111/1365-2478.12265.

Zhao, L., Qin, X., Zhang, J., Liu, X., Han, D.Hua, Geng, J., Xiong, Y., 2018. An effective reservoir parameter for seismic characterization of organic shale reservoir. Surv. Geophys. https://doi.org/10.1007/s10712-017-9456-9.